FUNCTIONALIZATION OF GROUP V MONOLAYERS AND THEIR COMPOUNDS: ALLOYING, DOPING AND SURFACE MODIFICATION

A DISSERTATION SUBMITTED TO

THE GRADUATE SCHOOL OF ENGINEERING AND SCIENCE

OF BILKENT UNIVERSITY

IN PARTIAL FULFILLMENT OF THE REQUIREMENTS FOR

THE DEGREE OF

DOCTOR OF PHILOSOPHY

IN

MATERIALS SCIENCE AND NANOTECHNOLOGY

By

Muammer Kanlı

November 2020

FUNCTIONALIZATION OF GROUP V MONOLAYERS AND THEIR COMPOUNDS: ALLOYING, DOPING AND SURFACE MODIFICATION

By Muammer Kanlı

November 2020

We certify that we have read this dissertation and that in our opinion it is fully adequate, in scope and in quality, as a dissertation for the degree of Doctor of Philosophy.

Engin Durgun(Advisor)

Ceyhun Bulutay

Cem Sevik

Hande Toffoli

Oğuz Gülseren

Approved for the Graduate School of Engineering and Science:

Ezhan Karaşan
Director of the Graduate School

ABSTRACT

FUNCTIONALIZATION OF GROUP V MONOLAYERS AND THEIR COMPOUNDS: ALLOYING, DOPING AND SURFACE MODIFICATION

Muammer Kanlı
Ph.D. in Materials Science and Nanotechnology
Advisor: Engin Durgun
November 2020

There has been growing interest during the last decade in two-dimensional (2D) materials due to their important roles in various scientific and technological applications such as detectors, lasers and light emitting diodes. In this thesis we present a theoretical investigation of a couple of such 2D materials from group V monolayers and their compounds. Firstly, ordered alloys of $Ga_xAl_{1-x}N$ hexagonal monolayer are studied and the effect of Al content on mechanical, electronic, thermal and optical properties are investigated. The optimized lattice constants and band gaps change in accordance to Vegard's Law. Low barrier energies and favorable substitution of Ga by Al may show feasibility of fabrication. Segregation is also checked with mixing energy calculations. The dynamical stability of alloys is shown by phonon spectrum analysis and MD simulations. $Ga_xAl_{1-x}N$ alloys give lower in-plane stiffness than h-BN or graphene, but higher Poisson's ratio than most realized 2D systems. Heat capacity of alloys delivers a decrease with Al content at low temperatures but it converges to the classical limit at high temperatures. The absorption onset of $Ga_xAl_{1-x}N$ alloys remain in the near UV range and prominent absorption peaks blue-shifts with increasing x in compliance with the variation of the band gap. The considered systems, in regard to their stability and tunable fundamental properties seem to be very promising 2D semiconductors for wide range of applications at reduced scales. Then, the interaction of alkali metal atoms (Li, Na, and K) with single layer and periodic structures of *hb*-As and *sw*-As phases are revealed by first-principles methods. Arsenene phases are considered to be used as electrodes (anode) for ion-batteries. Strong alkali-electrode binding and low diffusion energy barriers gives out better cycling stability and faster diffusion, respectively. *hb*-As shows better storage capacity than *sw*-As. However, deviations from ordered pattern and decline of formation energy with increasing doping level point out a possible structural transformation. By MD calculations, crystalline to amorphous phase transition is seen even

for low concentrations level at ambient temperature. The average open-circuit voltages of 0.68-0.88 V (0.65-0.98 V) with specific capacity up to 715 $mAhg^{-1}$ (358 $mAhg^{-1}$) are calculated for single layer (periodic) configurations. Overall, non-crystalline phases are calculated to offer more favorable structures than crystalline configurations and they provide more coherent results when compared with experimental data. The obtained voltage profile together with low diffusion barriers and strong metal-electrode binding suggests arsenene as a promising anode material to be used in for alkali-ion battery applications. Lastly, the formation of dumbbell (DB) geometry upon adsorption of Ga, N adatoms to GaN monolayer is investigated. While Ga-N DBs are unstable, Ga-Ga and N-N DB geometries are predicted to form in an exothermic and spontaneous scheme. Cohesive energy of hexagonal GaN monolayer decreases when a DB is formed on its surface. Electronic structures for Ga-Ga DBs for 2×2, 3×3, 4×4 and 5×5 phases show spin-polarized and degenerate bands mainly contributed by p-orbitals of the atoms in impurity zone. Degenarated bands are not observed for N-N dumbbell for HDP, TDP, 2×2 and 3×3 phases. Upon DB formation, semiconductor GaN monolayer become spin-polarized semiconductor with varying band gap, where this functionalization allows electronic structure to be tuned substantionally. This would be highly desired for nanoscale electronic and optical devices. These Ga-Ga and N-N DB geometries may also be used for the synthesis of layered GaN structures.

Keywords: First principles, ab initio, density functional theory (DFT), nanostructures, monolayer, phonon, electronic properties, doping, 2D materials, GaN, AlN, arsenene, dumbbell.

ÖZET

TEK TABAKA GRUP V SİSTEM VE BİLEŞİKLERİNİN FONKSİYONELLEŞTİRİLMESİ: ALAŞIM, KATKI VE YÜZEY MODİFİKASYONU

Muammer Kanlı
Malzeme Bilimi ve Nanoteknoloji, Doktora
Tez Danışmanı: Engin Durgun
Kasım 2020

Son onbeş-yirmi yıldır dedektör, laser ve LED gibi birçok bilimsel ve teknolojik uygulamalardaki önemli rolleri sebebiyle iki boyutlu (2B) malzemeler artan bir ilgiyle araştırılmaya devam etmektedir. Bu tez çalışmasında grup V ve bileşikleri arasından tek tabaka yapısına sahip birkaç malzeme üzerinde teorik bir çalışma yapıldı. İlk çalışmada altıgen örülü $Ga_xAl_{1-x}N$ düzenli alaşım tek tabakası üzerinde Al içeriğinin bu alaşımlara ait mekanik, elektronik, termal ve optik özelliklere etkisi araştırıldı. Optimize edilmiş örgü sabiti ve bant aralıkları Vegard kanununa uygun bir şekilde değişmektedir. Düşük bariyer enerjisi ve enerji-elverişli Al→Ga değişimi bu alaşımların üretilebileceğini göstermektedir. Karışım enerjisi hesapları yapılarak kristal yapıda ayrışma olmadığı gösterilmiştir. Phonon spektrum analizi ve MD simülasyonları yapılarak alaşımların dinamik olarak stabil kaldıkları gösterilmiştir. $Ga_xAl_{1-x}N$ alaşımları h-BN veya grafene göre daha düşük düzlem-içi sertlik değerine sahipken birçok iki boyutlu malzemeye göre daha yüksek Poisson oranı göstermektedir. Düşük sıcaklıklarda Al içeriğine bağlı bir düşme gösteren ısı kapasitesi yüksek sıcaklıklarda ise klasik limit değerine yakınsamaktadır. $Ga_xAl_{1-x}N$ alaşımların absorpsiyon başlangıç değerleri yakın UV bölgesinde kalmakta ve x arttıça belirgin absorpsiyon tepe noktaları bant aralığı değişimiyle uyum göstererek maviye kaymaktadır. Stabil olmaları ve ayarlanabilir temel özellikleri bu alaşım sistemlerini geniş bir uygulama alanında ümit veren iki boyutlu malzemeler arasında sokmaktadır. İkinci çalışmada alkali metal atomların (Li, Na ve K) tek tabakalı veya periyodik *hb*-As ve *sw*-As fazlı yapılarla etkileşimleri incelenmiştir. Arsenene fazlarının ion-pillerde elektrot (anot) olarak kullanılabilecekleri düşünülmektedir. İlk prensiplere dayalı yapılan hesaplarda ortaya çıkan güçlü alkali-elektrot bağları ve elektrot üzerinde alkaliler için düşük diffüzyon enerji bariyer değerleri bu pillerin daha iyi döngüsel stabiliteye sahip olduklarını ve daha hızlı diffüzyona izin verdiklerini göstermektedir.

hb-As fazı diğer faza göre daha iyi depolama yeteneğine sahiptir. Ancak düzenli desenden sapmalar görülmesi ve doping miktarı arttıkça formasyon enerjisinin düşme göstermesi yapısal dönüşümlerin olabileceğini göstermiştir. MD hesap sonuçları, kristal yapının düşük konsantrasyonlarda ve hatta oda sıcaklığında bile amorf yapıya dönüştüğünü göstermektedir. Tek tabakalı (periyodik) konfigürasyonlarda en yüksek 715 $\mathrm{mAhg^{-1}}$ (358 $\mathrm{mAhg^{-1}}$) spesifik kapasite değeri için ortalama açık devre voltajları 0.68-0.88 V (0.65-0.98 V) olarak hesaplanmıştır. Kristal olmayan yapıların genel olarak daha uygun bir konfigürasyona sahip oldukları ve deneysel sonuçlara daha uyumlu özellikler gösterdikleri belirlenmiştir. Elde edilen voltaj profili, düşük difüzyon bariyerleri ve güçlü metal-elektrot bağları birlikte düşünüldüğünde iki boyutlu arsenenenin alkali-ion piller uygulanabilecek ümit veren bir anot malzemesi olarak kullanılabileceği görünmektedir.

Son olarak altıgen örülü GaN tek tabakası üzerine Ga, N atomları adsorpsiyonu sonucunda oluşan dambıl (DB) yapı incelendi. GaN ile stabil bir yapı oluşturan Ga-Ga ve N-N DB geometrileri ekzotermik ve spontane bir şekilde oluşmaktadır. Üzerinde DB oluşması, GaN tek tabaka kristal yapının kohezif enejisini azaltmıştır. 2×2, 3×3, 4×4 and 5×5 fazlar için Ga-Ga DB + GaN tabaka sistemlerin elektronik yapılarında spin-polarize ve dejenere bantlar oluşmaktadır, ki bu bantlar ağırlıklı olarak empürite bölgesindeki atomların p-orbitallerin katılımıyla oluşurlar. HDP, TDP, 2×2 ve 3×3 fazlar için N-N DB içeren sistemlerin elektronik yapılarında dejenere bantlar gözlenmemiştir. DB oluşumu, yarı iletken olan GaN tek tabakasını değişken bant aralıklı spin-polarize bir yarı iletken malzeme haline getirir. Bu modifikasyon, büyük miktarda ayarlanabilir bir elektronik yapı oluşumuna izin vermektedir, ki bu nanoölçekli elektronik ve optik cihazlar için aranılan bir özelliktir. Tabakalı GaN yapıların üretilmesinde Ga-Ga ve N-N DB oluşumlarından faydalanılabilir.

Anahtar sözcükler: İlk prensipler, ab initio, yoğunluk fonksiyoneli teorisi (YFT), nanoyapılar, tek tabaka, fonon, elektronik özellikler, katkılama, 2B malzemeler, GaN, AlN, arsenene, dambıl.

Acknowledgement

I am grateful to my supervisor Assoc. Dr. Engin Durgun for his guidance and support during my doctorate study. I would like to thank Prof. Dr. Ceyhun Bulutay and Prof. Dr. Cem Sevik for their invaluable advices, tips and fruitful discussions that were very beneficial for development of this thesis. I feel proud of being a member of condensed matter physics which stands on more than a century, dealing with material simulation.

I benefited so much from lecture notes (PHYS 741: Principles of Density Functional Theory) by Assoc. Dr. Hande Toffoli for the fundamentals of DFT method.

I am sincerely grateful to all of my friends and group members including Murat Serhatlıoğlu, Ali Kalantarifard, Gökay Günacar, Abdullatif Önen, Dr. Semran İpek, Dr. Berna Akgenç, Jamoliddin Khanifaev, Dr. Burak Özdemir, Mert Miraç Çiçek, Dr. Merve Demirtaş, Doğukan Hazar Özbey, Mohammad Abboud and Mirali Jahangirzadeh for their kind help, friendship, moral support and colorful contributions during my master and doctorate studies.

Finally I would like to thank my wife Şehnaz and daughter Melisa for their love and continuous support. I am profoundly indebted to my mom Emriye and dad Şakir for their full support constantly through my life.

This work was supported by the Scientific and Technological Research Council of Turkey (TUBITAK) under Project No 117F241.

Contents

List of Figures

List of Tables

Chapter 1

Introduction

Dimensionality is a very effective parameter in establishing the properties of a material. A two-dimensional (2D) structure shows many novel properties because of quantum confinement effects emerging from dimensional restriction [2–4]. After the exfoliation of monolayer carbon phase of graphene [5], 2D ultra-thin materials have attracted an enormous attention for scientific and technological innovations [6–10]. New, more efficient materials are researched for conventional technologies/applications [11–17].

Group III-nitrides (group III-N) are semiconductors having tunable band gaps that span from the infrared to ultraviolet [18]. Diverse applications for nanoelectronic and optoelectronic devices have been achieved using group III-nitrides, including photovoltaics [19–22], power electronics [23,24], detectors [25–28], light emitting diodes [29–33] and lasers [34–37]. This made group III-N materials one of the most important semiconductor families. Wide application range of their 3D crytals has opened the way for designing monolayer systems of group III-N compounds. BN, AlN, GaN and InN systems were calculated by *ab initio* methods [7, 9, 38–41], where they have stable graphene-like planar honeycomb structures but with wide band gaps and show exceptional electronic and optical properties, peculiar to their 2D structures. Experimental realization of BN, AlN and GaN have also been shown [42–45].

High performance field effect transistors (FET) fabricated from phosphorene have led significant interests on monoelemental pnictogens [46–60]. Their novel and diverse properties suggest pnictogens as suitable materials for various technological applications including but not limited to electrochemical batteries [61–65], thermoelectric devices [66, 67], and thin film solar cells [68–71]. Portable electronic and electrical vehicle industries crucially need rechargeable alkali-ion batteries, where the development of cathode material from cobalt oxide marked an important beginning step for their application on laptops and smartphones and honoured its inventor with Nobel Prize for Chemistry in 2019 [72]. For these applications, pnictogens can also be used as a potential electrode material. Fast/directional diffusion, good electrical conductivity, high/reversible capacity, and structural stability are some of the necessary characteristics that are highly desired from battery electrode materials. Numerous studies have investigated alkali metal-pnictogen interaction for this opportunity [65, 73–80]. Their larger accessible areas make 2D pnictogens very tempting materials for battery applications.

Functionalizations, namely introducing vacancies, doping, lateral/vertical heterostructures and straining can be applied on 2D crystals to modify their mechanical, electronic and magnetic properties [81–92]. Dumbbells (DB) have generally been predicted only as a geometrical form of adsorption, and not specifically described. This interesting structure was investigated in detail for group IV monolayers, where stable DB geometry was shown to form upon Ge/Si adsorption on germanene/silicene crystals, in exothermic and spontaneous scheme [93–95]. These new phases were shown to have diverse electronic and magnetic properties, tunable with varying DB coverage. Graphitic Si or Ge multilayer synthesis was proposed by stacking these dumbbell-including monolayers on top of each other. Germanene and silicene systems, utilized for DB formation are buckled and unary. Except BP monolayer, binary systems having planar geometry have not been investigated yet. DB formation upon Ga or N adsorption to GaN monolayer may produce tunable electronic, magnetic properties, which is highly desired for nanoscale electronic and optical devices. These geometries may also be used for the synthesis of layered GaN structures.

This brief introduction continues with Chapter II, where density functional theory and its methodology are explained. In Chapter III the fundamental properties of $Ga_{1-x}Al_xN$ ordered alloys in 2D hexagonal form are examined. The interaction of alkali metals with arsenene phases (*hb*-As and *sw*-As) are investigated in Chapter IV. Dumbbell formation as a new phase over GaN monolayer is studied in Chapter V. Finally, brief summary of results is given in Chapter VI, Conclusion part.

Chapter 2

Computational Method

2.1 Ab Inito Calculations and Density Functional Theory

Properties of matter can be predicted by considering the interaction of its building blocks, namely electrons and nuclei. Total energy of system, once calculated can be used to determine nearly all of the system's properties, or observables. Schrödinger published his famous paper dated 1926 [96], offering an equation that solves for the many-body interactions in the system, which can be used to find out the total energy:

$$\hat{H}\Psi_i(\mathbf{R},\mathbf{r},\mathbf{t}) = E_i\Psi_i(\mathbf{R},\mathbf{r},\mathbf{t}) \tag{2.1}$$

Here wave function, Ψ is the most complete quantum mechanical description of a physical system, while Hamiltonian operator, $\hat{H}$ describes its potential energy:

$$\hat{H} = \hat{T}_n + \hat{T}_e + \hat{V}_{nn} + \hat{V}_{ee} + \hat{V}_{ne} \tag{2.2}$$
$$= \sum_I^{N_n} \frac{\vec{P_I}^2}{2M_I} + \sum_i^{N_e} \frac{\vec{p_i}^2}{2m_e} + \frac{e^2}{4\pi\epsilon_0}\left[\sum_{I,J\neq I}^{N_n,N_n} \frac{Z_I Z_J}{|\vec{R_I} - \vec{R_J}|} + \sum_{i,j\neq i}^{N_e,N_e} \frac{1}{|\vec{r_i} - \vec{r_j}|} + \sum_{i,I}^{N_e,N_n} \frac{Z_I}{|\vec{r_i} - \vec{R_I}|}\right]$$

The possible outcome of this equation inspired Dirac to proclaim the end of chemistry. However the system is composed of many-bodies having electrostatic

correlations between each other, where the unknown parameters needed for solution is $3N_n + 3N_e$. The number of unknowns show that this equation can not be solved exactly, except only for simple systems like H or He. Therefore approximations were made, by wavefunction-based (perturbational or variational) or density-based (Thomas-Fermi Approximation [97, 98] or Density Functional Theory (DFT) methods.

In the development of DFT to have a reliable outcome for systems being more complex than H or He, some approximations were developed. Born-Oppenheimer [99], relying on quite smaller mass of electron with respect to that of nucleus considered an instantaneous follow-up electron motion upon the movement of nuclei. By this approximation, the total wave function $\Psi(\mathbf{R}, \mathbf{r}, \mathbf{t})$ is reduced to electronic wave function $\Phi(\mathbf{r})$ and many-body electronic Schrödinger equation without $\hat{T}_n$ remains to be solved for fixed nuclei positions (2.3). Another approximation was made by Hartree [100] who factorized many-electron wave function as the product of one-electron wave functions (2.4). An improvement came by Hartree-Fock approximations [101, 102], which includes electron spin and build up the wave function in antisymmetric form, namely Slater determinant (2.5).

$$\Psi(\mathbf{R}, \mathbf{r}, \mathbf{t}) = \Theta(\mathbf{R}, \mathbf{t})\Phi(\mathbf{R}, \mathbf{r}) = \Theta(\mathbf{R}, \mathbf{t})\Phi(\mathbf{r}) \tag{2.3}$$

$$\Phi(\mathbf{r}) = \phi(\mathbf{r_1})\phi(\mathbf{r_2}) \cdots \phi(\mathbf{r_N}) \tag{2.4}$$

$$\Phi(\mathbf{r}) = \frac{1}{\sqrt{N!}} \begin{vmatrix} \phi_1(\mathbf{r_1}) & \phi_2(\mathbf{r_1}) & \cdots & \phi_N(\mathbf{r_1}) \\ \phi_1(\mathbf{r_2}) & \phi_2(\mathbf{r_2}) & \cdots & \phi_N(\mathbf{r_2}) \\ \vdots & \vdots & \ddots & \vdots \\ \phi_1(\mathbf{r_N}) & \phi_2(\mathbf{r_N}) & \cdots & \phi_N(\mathbf{r_N}) \end{vmatrix} \tag{2.5}$$

Here each electron orbital is calculated to describe the system. In Thomas-Fermi method, non-interacting electrons comprising homogeneous gas with local density was used. Later Dirac included exchange-correlation interactions into this method.

Hohenberg-Kohn formed the basis of DFT by their two simple theorems in 1964 [103]. The first theorem states for any system of interacting particles in an

external potential that its electronic density is uniquely determined. The second theorem defines the energy functional in terms of density and provides the ground state density by minimizing this functional. All of the physical properties can be calculated by using ground state density. These theorems were further developed and the Schrödinger equation was modified into a solvable version by Kohn and his postdoc Sham in 1965 (KS) [104], by transforming an intractable many-body of interacting electrons in static external potential into a noninteracting state with an effective potential (V_{eff}) term. V_{eff} comprises three terms, *external*, *Hartree* and *exchange-correlation* potentials, as shown (eq 2.7) respectively. V_{ext} accounts for electron-nuclei interaction, V_H calculates electron-electron interaction and V_{XC} justifies the difference between interacting and non-interacting electrons.

$$\Big(-\frac{\hbar^2}{2m_e}\nabla^2 + V_{eff}(\mathbf{R},\mathbf{r})\Big)\phi_i(\mathbf{r}) = \epsilon_i\phi_i(\mathbf{r}) \tag{2.6}$$

where the effective potential is defined as follows:

$$V_{eff}(\mathbf{R},\mathbf{r}) = V_{ext}(\mathbf{R},\mathbf{r}) + V_H(\mathbf{r}) + V_{XC}(\mathbf{r}) \tag{2.7}$$

Till now, general frame for mapping many-body problem into equivalent single-particle problem is presented. This brings infinite number of non-interacting electrons moving in a static external potential formed by surrounding infinite number of nuclei and electrons. Wave functions, describing the states of electrons can be formed by superposition of plane waves (expansion) but theoretically an infinite basis set is needed for this. Considering the periodicity of solid and using Bloch's theorem [105] simplifies the formation of wave function and allows the usage of finite number of plane waves. The theorem breaks down the wave function into a lattice periodic function and a phase factor (wavelike part) and reduces the Hamiltonian into wavevector-dependent form.

Solids are finite materials that have surfaces. They are formed by huge numbers of particles (electrons, nuclei) in a periodic lattice. This makes crystals infinite systems with specific boundary conditions. Lattice periodicity enforces any property or function defined for a crystal to be translationally symmetric. Fourier

transform handles such functions very easily. Under the condition of $e^{\mathbf{q}\cdot\mathbf{a}_i} = 1 \Rightarrow$ $\mathbf{q}\cdot\mathbf{a}_i = 2\pi m$ (m is integer) the real space is transformed into the reciprocal space ($\mathbf{r}\rightarrow\mathbf{q}$), where Fourier components of such systems can be used for the analysis rather than working them in real space. Here, $\mathbf{T} = \sum n_i\mathbf{a}_i$ and $\mathbf{G} = \sum n_i\mathbf{b}_i$ are the translation vectors for real and reciprocal spaces, respectively. Eq 2.8 presents partitioning of the wave function and eq 2.9 gives the basis set expansion of its lattice periodic part, as shown below. These equations can be combined to obtain plane wave representation of the electronic wave function.

$$\phi_i(\mathbf{r}) = u_i(\mathbf{r})e^{i\mathbf{k}\cdot\mathbf{r}} \tag{2.8}$$

$$u_i(\mathbf{r}) = \sum_G c_{i,G}e^{i\mathbf{G}\cdot\mathbf{r}} \tag{2.9}$$

Application of boundary conditions over the solid specifies a set of **k**-points where electronic states are calculated. This set of 'allowed' **k**-points are used to discretize domain (volume). Density of **k**-points is proportional with the volume. (This is inverse if the calculations are carried out in reciprocal space where Fourier transform is used) Finite number of wave functions need to be calculated at infinite number of **k**-points. Because of the contributions coming from each **k**-point, an infinite number of calculations are required to compoute the electronic potential in the bulk solid. But almost identical wave functions are obtained at **k**-points having close proximity, which allows particular region of **k**-space to be represented by a single **k**-point. Using these methods, the electronic potential and total energy can be accessed with an accuracy using a finite set of **k**-points.

Bloch's method introduces a discretized plane-wave basis set for wave function expansion. For this, it principally needs to incorporate infinite basis set. However, the contributions of plane-waves with high kinetic energy are less significant than those with small kinetic energy. A cutoff energy can be determined, which allows a truncation in plane-wave basis set. Thus the infinite basis set can be reduced to a finite size. The error created by this truncation can be lowered by increasing the cutoff energy until the total energy is converged.

When wave functions are expanded with basis sets, Kohn-Sham equations are transformed into a simpler form (Eq 2.10), where the kinetic energy is diagonal

and Fourier transform is used to calculate the potentials. Hamiltonian matrix can be diagonalized for the solution. The cutoff energy choice will determine the matrix size.

$$\sum_{G'} \Big[\frac{\hbar^2}{2m_e} |\mathbf{k}+\mathbf{G}|^2 \delta_{\mathbf{G}\mathbf{G}'} + V_{eff}(\mathbf{R},\mathbf{r})(\mathbf{G}-\mathbf{G}') \Big] c_{i,\mathbf{k}+\mathbf{G}'} = \epsilon_i c_{i,\mathbf{k}+\mathbf{G}'} \tag{2.10}$$

At this point the all-electron system including core and valence electrons still has many electronic wave functions to be determined. This problem can be alleviated by pseudopotential method which is explained in later section. By this approach we have limited number of electrons for which small number of grids of domain can be utilized for their plane-wave expansion. However, there are still too many interdependent unknowns. As pointed out previously, DFT method forms density and energy functional, as a new variable and dependent variable, respectively and minimizes the total energy functional to determine the ground state of the system. In this way the number of unknowns is reduced from 3N to 3, N referring to the total number of valence electrons of the system. Electronic density is defined with only three spatial coordinates. Here DFT changes the nature of electronic wave functions that are described to define the state of each electrons of the system, and transforms them into a set of states (KS orbitals) describing the electronic density.

When the total energy is represented in terms of density, the following KS Hamiltonian is obtained:

$$\begin{aligned} H_{KS} = -\frac{\hbar}{2m_e} \sum_i^{N_e} \int \phi_i^*(\mathbf{r}) \nabla^2 \phi_i(\mathbf{r}) d\mathbf{r} + \int \rho(\mathbf{r}) \hat{V}_{ne} d\mathbf{r} \\ + \frac{1}{2} \int\int \frac{\rho(\mathbf{r})\rho(\mathbf{r}')}{|\mathbf{r}-\mathbf{r}'|} d\mathbf{r} d\mathbf{r}' + \int \rho(\mathbf{r}) \epsilon_{XC}(\rho(\mathbf{r}) d\mathbf{r} \end{aligned} \tag{2.11}$$

where its terms correspond to kinetic energy, external potential, Hartree and exchange-correlation energies, respectively, and

$$\rho(\mathbf{r}) = \sum_i^{N_e} f_i \big| \phi_i(\mathbf{r}) \big|^2 \tag{2.12}$$

electronic density (ρ) is calculated by summing the multiplication of occupations with corresponding orbital squares.

The basic steps of self-consistent DFT calculations are given above. The procedure is applied in the following way: For an assumed ionic configuration, an initial guess for electron density is made. This value is used to calculate V_{eff}. Then KS equations (eq 2.11) are used to determine the electronic wave functions (KS orbitals), which are used with eq 2.12 to calculate a new electron density. Comparison is made between consecutive electron density values. For self-consistency, the iteration continues until the difference is below an acceptable value. After the electronic density is converged (ground state density), observables (total energy, force, charge density etc.) are calculated.

2.2 Exchange-Correlation Functionals

Referring to Kohn-Sham Hamiltonian (eq 2.11), only the last term (correction) needs to be addressed with respect to density. This correction sums exchange energy for Pauli repulsion (which is ignored in Hartree term) and correlation energy for electron-electron repulsion, respectively. Several approximations were developed for this sum.

2.2.1 Local Density Approximation (LDA)

As Kohn-Sham presented, solids can be assumed to have homogeneous electron gas system, for which its inhomogeneous electronic system is considered to be locally homogeneous and exchange-correlation effects are characterized locally. With this principle, the oldest exchange-correlation functional LDA [106, 107] calculates E_{XC} by summing explicit exchange and approximate correlation corrections. For polarized systems, electron spins are included and Local Spin Density Approximation (LSDA) can be used as the most general local approximation. In spite of its overbinding in molecules and solids, LDA works remarkably well and calculates the chemical trends correctly. Its success made it the starting point for developing improved functionals.

2.2.2 Generalized Gradient Approximation (GGA)

Systems are inhomogeneous in reality, owing to spatial variation of electric field created by nuclei and electrons' screening. New and better density representation methods, namely generalized gradient approximations (GGA) [108] are developed by imposing gradient on homogeneous density of LDA. Various analysis like binding energy, atomic energy, chemical reaction energetics and bond lengths can be performed by DFT method with the higher accuracy gained by this method.

2.2.3 Hybrid Functionals

Hartree term unphysically includes self-interaction of electrons. LDA or GGA can not compansate for this error. In the calculated electronic band structure, occupied states are pushed upwards by this unphysical energy contribution. This results in a band gap reduction, as seen in Fig. 2.1. Becke [109] introduced an hybrid approach to construct E_{XC} term by a linear combination of Hartree-Fock's exact exchange functional and any number of exchange and correlation functionals, that are calculated using LDA or GGA aprroaches. Weight parameters for this combination are determined by fitting the predictions of functionals to experimental or accurately calculated thermochemical data. To improve computational efficiency, hybrid method calculates the exchange term by using error-function-screened Coulomb potential. Three popular hybrid XC functionals are calculated as follows:

$$\begin{aligned} E_{\mathrm{xc}}^{\mathrm{PBE0}} &= 0.25E_{\mathrm{x}}^{\mathrm{HF}} + 0.75E_{\mathrm{x}}^{\mathrm{PBE}} + E_{\mathrm{c}}^{\mathrm{PBE}} \\ E_{\mathrm{xc}}^{\mathrm{HSE}} &= aE_{\mathrm{x}}^{\mathrm{HF,SR}}(w) + (1-a)E_{\mathrm{x}}^{\mathrm{PBE,SR}}(w) + E_{\mathrm{x}}^{\mathrm{PBE,LR}}(w) + E_{\mathrm{c}}^{\mathrm{PBE}} \end{aligned} \tag{2.13}$$

where for PBE0 a combination of exact HF and PBE and for HSE a combination of exact HF and PBE with Coulombic interaction screening are used. HSE functionals lead better band gap calculation, where HF and PBE are mixed with parameter a, while the range of interaction is screened by w. HF,SR and PBE,LR refer to short-range Hartree-Fock and long-range component of PBE, respectively. HSE06 functional using a=0.25 and w=0.2 parameters gives good results for most

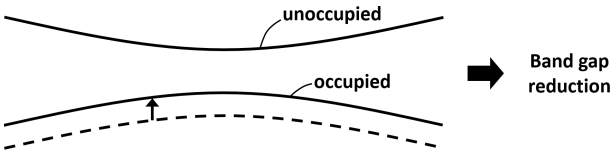

Figure 2.1: Band gap reduction caused by Hartree term in Kohn-Sham Hamiltonian. This error can not be corrected by LDA or GGA functionals.

systems.

2.3 Pseudopotential Approximation

Too slow decay of all-electron (Full Coulomb potential) calculation for electron-ion interaction drives DFT research to make another approximation, which can be briefly explained in the following way: An atom in a solid or molecule system is composed of an ion core and valence electrons, where former involve nuclei and tightly bound core electrons. All-electron method treats core and valence electrons on an equal footing, which results in the above mentioned slow decay. Instead, pseudopotential approach considers a frozen ion core. This method calculates the system properties with the assumption that the ion cores are not involved in chemical bonding and do not change as a result of structural modifications. This approximation for the ionic wave function and potential can be seen in Fig. 2.2. Orthogonality constraint forces exact all-electron wave functions to oscillate rapidly in the core region, which can be followed only by vast number of plane waves. This puts burden on the solutions of KS equationsTo follow the rapid change of tightly bound core orbitals

Plane wave representation of this function is numerically inefficient. Instead of exact approach dealing with all electrons, pseudopotential method replaces core electrons and strong Coulomb potential (V) with a weak pseudopotential (V_{pseudo}) acting on a set of pseudo wave functions (Ψ_{pseudo}). In addition to this, it has been shown that most of the physical properties of solids are heavily dependent on the valence electrons, i.e. core electrons do not have significant effect for this respect.

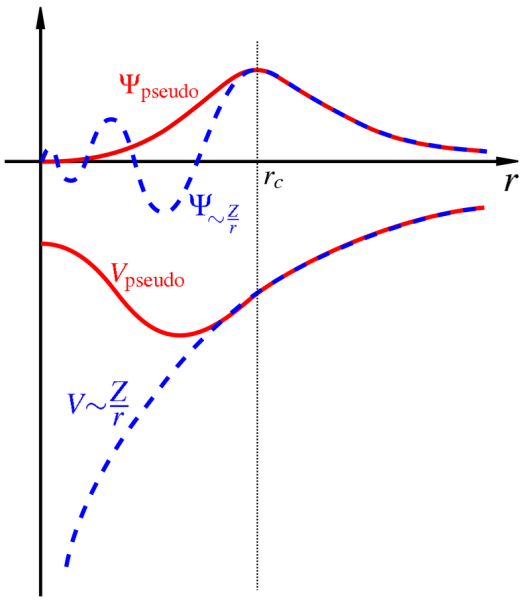

Figure 2.2: Comparison of a wave function (Ψ) in the Coulomb potential (V) of the nucleus (blue dashed) to the one in the pseudopotential (red solid). The real and the pseudo wave function and potentials match above a certain cutoff radius, r_c. Figure is taken from Ref [1].

Pseudopotential method requires the core electron states to be precalculated in atomic environment and kept frozen for further calculations. Pseudopotentials can be formed in three ways: **norm conserving**, **ultrasoft (UPSS)** and **projector augmented wave (PAW)**. For the generalized norm conserving pseudpotentials [110], charge within the cut-off sphere is kept fixed. Vanderbilt developed UPSS [111] by forming non-local potential that involves smooth pseudo-wavefunction. PAW method, similar to UPSS reconstructs exact wave functions of the core region by introducing projectors and auxiliary localized functions. PAW approach aims the combination of the accuracy of all-electron method with the efficiency of pseudopotentials. UPSS and PAW methods are not norm conserving.

2.4 Phonons and Molecular Dynamics (MD) Calculations

The stability of crystal structure can be tested statically or dynamically. Former is implemented in finding the global energy minimum for total energy of the system, where *ab initio* DFT theory is used to relax the lattice structure by varying positions, dimensions and angles. Latter method involves phonon or high-temperature molecular dynamics (MD) calculations. In this thesis, the phonon spectra is calculated within the DFT framework by density functional perturbation theory (DFPT). Hellman-Feynmann theorem [112] allows the calculation of the ionic forces and the stress tensor by:

$$F_i = \frac{dE}{dR_i} \quad \text{and} \quad C_{ij} = \frac{dF}{dR_j} \tag{2.14}$$

where E, F_i, and C_{ij} correspond to total energy of the system, force on nucleus, and interatomic force constant. By using these parameters dielectric constant(ϵ_2), specific heat (C_v), effective charges and electron-phonon interactions can be calculated. DFPT method was developed to determine the phonon spectra of systems of ionic compounds (including charge localizations), to correctly calculate the LO-TO splitting.

As a further step for resolving the stability of structure, *ab initio* molecular dynamics (MD) calculation is carried out to investigate the effect of temperature on the lattice structure. MD can be performed by using microcanonical ensemble at a finite temperatures with scaled velocity approach (keeping temperature constant) with time steps for total simulation time, which is long enough to see the effect of the temperature. For this analysis, supercell is used to remove the unitcell constraint.

2.5 Inclusion of van der Waals (vdW) Forces

Stemming from mutual dynamical polarization of interacting atoms, vdW interactions can not be described accurately by density functionals. Thus semi-empirical methods are used to implement this interaction successfully into the calculations. In DFT-D3 method with Becke-Johnson (BJ) damping that makes atom pairwise additive treatment, the previous method with zero damping is revised and empirical energy correction (eq 2.16) is added to conventional self-consistent DFT energy functional.

$$E_{disp} = -\frac{1}{2}\sum_{I=1}^{N_{at}-1}\sum_{J=I+1}^{N_{at}}\sum_{L}\left(f_{damp,6}(R_{IJ,L})\frac{C_{6IJ}}{R_{IJ,L}^{6}} + f_{damp,8}(R_{IJ,L})\frac{C_{8IJ}}{R_{IJ,L}^{8}}\right) \quad (2.15)$$

where $L = (l_1, l_2, l_3)$ represents translations of the unit cell, C_{n8IJ} are geometry-dependent dispersion coefficients adapted by coordination number and BJ-damping function, $f_{damp,n}(R_{IJ,L})$ is calculated by the following form:

$$f_{damp,n}(R_{IJ}) = \frac{s_n R_{IJ}^n}{R_{IJ}^n + (a_1 R_{0IJ} + a_2)^n} \quad (2.16)$$

where a_1, a_2 and s_8 are free fit parameters, s_6=1 for GGA and hybrid functionals and s_8 is used to adapt the correction to the repulsive character of the short/medium-range behavior of the XC functional.

Illustrative atomic layout and some terms used for this E_{disp} summation are demonstrated in Fig. 2.3.

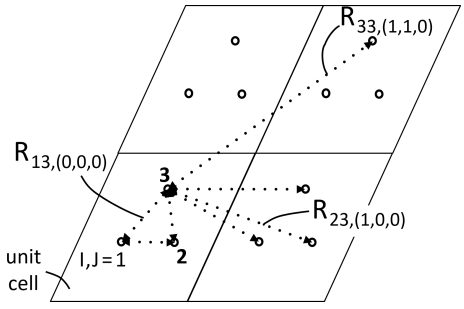

Figure 2.3: Atomic layout that can be used to formulate energy correction to calculate vdW interaction.

Chapter 3

2D $Ga_{1-x}Al_xN$ Ordered Alloys

Part of this chapter was published as; M. Kanli, A.Onan, A.Mogulkoc, E. Durgun, Characterization of two-dimensional $Ga_{1-x}Al_xN$ ordered alloys with varying chemical composition, Computational Materials Science 167 (2019): 13-18 [10].

3.1 Introduction

Hexagonal monolayers of h-GaN and h-AlN are wide band gap semiconductors with exceptional properties which have been revealed in extensive studies [113]. For instance, their 2D sheets, decorated with H or F atoms have been explored and their ferromagnetic and half-metallic characteristics have been pointed out [114]. The tunable electronic properties of 2D group III-nitride heterostructures have been investigated and their potential applications including solar cells have been suggested [88, 115–118]. Chemical functionalization of GaN [90] and AlN [119] monolayers with various adatoms have been shown to provide novel electronic and magnetic properties.

The applications of 2D semiconductors, in specific group III-nitrides are limited by scalability and/or formability issues, and also controllable modification of their (opto-) electronic properties [40]. Alloying offers a promising strategy,

since band gap of bulk semiconductors can be directly controlled with constituent composition [120–122]. Even though alloying in 2D is different from bulk systems due to dimensionality effects and boundary conditions [115, 123, 124], this approach is recently realized for 2D transition metal dichalcogenide (TMD) alloys and $Mo_{1-x}W_xS_21001$[116], $Mo_{1-x}W_xSe_21001$[125, 126], $andMoS_{2(x)}Se_{2(1-x)}$ [127] have been synthesized within this class. These systems have been analyzed in detail and their tunable optical properties have been demonstrated [116,128]. In addition to TMDs, hexagonal boron-carbon-nitride (h-BC_xN) composites have been examined by scanning tunneling microscopy to reveal the dynamics of mixing and order-disorder transitions which are crucial for growth of 2D alloys [129]. The alloys of 2D group IV systems ($Si_{1-x}C_x$, $Si_{1-x}Ge_x$, and $Ge_{1-x}C_x$) have been studied and the variation of their thermodynamic, structural, and electronic properties with composition have been explored [130]. The geometry and band structures of 2D SbBi alloy films have been studied by *ab initio* methods and their topological properties including topological phase transitions have been examined [131]. Among group III-nitrides, the fundamental properties of $In_xGa_{1-x}N$ alloys have been explored by first-principles calculations, and structural parameters, mixing enthalpies, and band gaps for different structures have been reported. Although bulk $Ga_{1-x}Al_xN$ have been synthesized [132, 133] and studied extensively [134], apart from studies on doping of 2D GaN with Al [135], alloys of GaN and AlN are not yet considered albeit their structural similarity and lattice match and also possibility of using them in various optoelectronic applications [116, 124].

Motivated with the recent synthesis of 2D GaN and AlN, and their potential implementation in nanoelectronics, we examine the fundamental properties of $Ga_{1-x}Al_xN$ ordered alloys [136, 137] in planar and hexagonal form, where x indicates the Al content. Starting from the pristine h-GaN and h-AlN which also set the end-points, optimized structures of alloys are obtained and cohesive/substitution energies are calculated. Following the analysis on phase segregation, the dynamic stability of the alloys is taken into account and is studied by phonon spectrum analysis and high temperature molecular dynamics (MD) simulations. Next, the variation of structural, mechanical, electronic, thermal, and optical properties of $Ga_{1-x}Al_xN$ alloys ($0 < x < 1$, 0.25 interval) are explored

and trends are revealed.

3.2 Method

Common references and parameters for Chapters 3,4,5: We performed first principles calculations using the Vienna Ab initio Simulation Package (VASP) [138–141] based on density functional theory (DFT). Projector-augmented wave (PAW) potentials [142, 143] were used to describe elements. The exchange-correlation functional was approximated by generalized gradient approximation (GGA) within Perdew, Burke, and Ernzerhof (PBE) scheme [144]. The atomic positions were optimized by using conjugate gradient method following the minimization of the total energy of the system. The energy and force convergence criteria between the two consecutive steps were taken to be 10^{-5} eV and 0.01 eV/Å, respectively. A super cell with a vacuum spacing of 20 was used to avoid spurious interaction between periodic images in adjacent cells. Lateral and vertical diffusion barriers were obtained with nudged elastic band (NEB) technique [145–147]. Phonon spectra of systems were calculated by Phonopy package [148] based on Density Functional Perturbation Theory (DFPT) implemented in VASP.

Plane-wave basis set with an energy cutoff of 520 eV was taken. The Brillouin zone of 2×2 super cell was sampled with 21×21×1 k-point mesh set by Monkhorst-Pack method [149]. The density derived electrostatic and chemical (DDEC) approach method was utilized for the analysis of interionic charge-transfer [150]. Following expressions are used for; cohesive energy,

$$E_c = (1-x)E_T(\mathrm{Ga}) + xE_T(\mathrm{Al}) + E_T(\mathrm{N}) - E_T(\mathrm{Ga}_{1-x}\mathrm{Al}_x\mathrm{N}) \tag{3.1}$$

average substitution energy,

$$E_{sub} = \frac{\left[xE_T(\mathrm{Al}) + E_T(\mathrm{GaN})\right] - \left[xE_T(\mathrm{Ga}) + E_T(\mathrm{Ga}_{1-x}\mathrm{Al}_x\mathrm{N})\right]}{x} \tag{3.2}$$

free energy of mixing,

$$F_{mix} = E_{mix}(x) - TS_{mix}(x) \tag{3.3}$$

internal energy of mixing,

$$E_{mix} = E_T(\mathrm{Ga}_{1-x}\mathrm{Al}_x\mathrm{N}) - (1-x)E_T(\mathrm{GaN}) - xE_T(\mathrm{AlN}) \tag{3.4}$$

and entropy of mixing,

$$S_{mix} = -nR\big[(1-x)\ln(1-x) + x\ln(x)\big] \tag{3.5}$$

where E_T(Ga), E_T(Al), E_T(N), E_T(GaN), E_T(AlN), and $E_T(\mathrm{Ga}_{1-x}\mathrm{Al}_x\mathrm{N})$ correspond to total energy of single Ga, single Al, single N, h-GaN, h-AlN, and $\mathrm{Ga}_{1-x}\mathrm{Al}_x\mathrm{N}$ alloy. R, n and T indicate gas constant, total mole of atoms (=2 for each alloy) and temperature, respectively. All energies are normalized to unit cell of pristine systems.

As fundamental band gaps are underestimated at GGA level, we also performed calculations with hybrid functionals (HSE06) [151, 152], which is formed by mixing 25% of the Fock exchange with 75% of the PBE exchange and 100% of the PBE correlation energy. The dynamical stability of the structures was further tested by *ab initio* molecular dynamics (MD) calculations using microcanonical ensemble by scaling the atomic velocities at 300 K, 600 K, and 900 K for 3 ps total simulation time. A larger super cell (6×6×1) was used for the stability analysis. The frequency dependent dielectric functions of the structures were calculated by using random phase approximation (RPA) within GGA-PBE with an increased k-point mesh of 117×117×1 and including a total number of 96 bands.

3.3 Results and discussione

3.3.1 Structural properties and energetics

We start from the pristine h-GaN and h-AlN systems, monolayers of which have stable, planar honeycomb structures with calculated lattice constants, a of 3.21 Å and 3.13 Å, respectively [7, 9, 39, 113]. Following the optimization of pristine structures, we design $\mathrm{Ga}_{1-x}\mathrm{Al}_x\mathrm{N}$ ordered alloys [136, 137] for

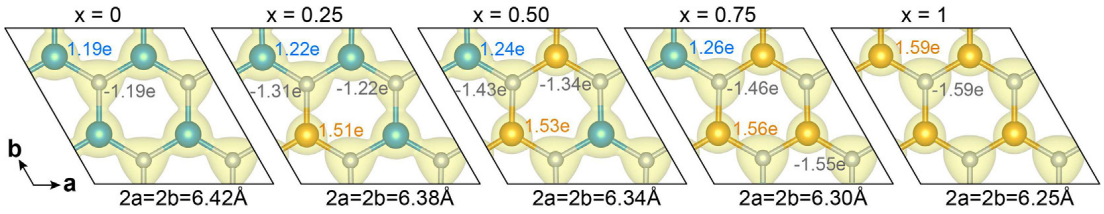

Figure 3.1: Top views of the optimized atomic structures of $Ga_{1-x}Al_xN$ alloys with bond charges. The 2×2 super cell (with respect to primitive unit cell of pristine system) are laid out by solid lines as 2D parallelogram. Turquoise, yellow, grey spheres stand for Ga, Al and N atoms, respectively. Lattice constants (a, b) and charge transfer are indicated for each system.

$x = 0, 0.25, 0.50, 0.75, 1$ where x refers to Al content. 2×2 super cell (with respect to primitive unit cell of bare systems) which is shown in Fig. 3.1 is considered. $Ga_{1-x}Al_xN$ has hexagonal lattice similar to pristine systems and optimized lattice constant, a decreases with increasing x following Vegard's Law [153, 154] as illustrated in Fig. 3.2(a).

Buckled geometries are also tested, however the planarity is preserved for all x values. Hybridization among sp^2 orbitals of cation (Ga or Al) and anion (N) form strong σ-bonds and perpendicular p_z orbitals form π-bonds which maintain the planar geometry. As expected there is a charge transfer (Q^*) from cation to anion atoms which is shown in Fig. 3.1 where positive (negative) values indicate charge donation (accumulation). The charge transferred to N gradually increases with increasing x which is correlated with the electronegativity difference between Al and Ga. Similar to a, the cohesive energy (E_c) of the alloy varies almost linearly with x and it increases with increasing Al content as presented in Fig. 3.2(b). Owing to similar geometry and lattice match, 2×2 super cell is tested to be sufficient to study the fundamental properties of the ordered patterns [155]. When calculations are repeated with 4×4 super cell with different arrangements of Al at specified x, same a values are obtained and E_c differs only up to ±10 meV.

One of the possible methods to manufacture such alloys is the chemical vapor deposition (CVD) technique and in that sense the energy required to substitute Ga with Al (E_{sub}) gives an indication about feasibility of the procedure. As

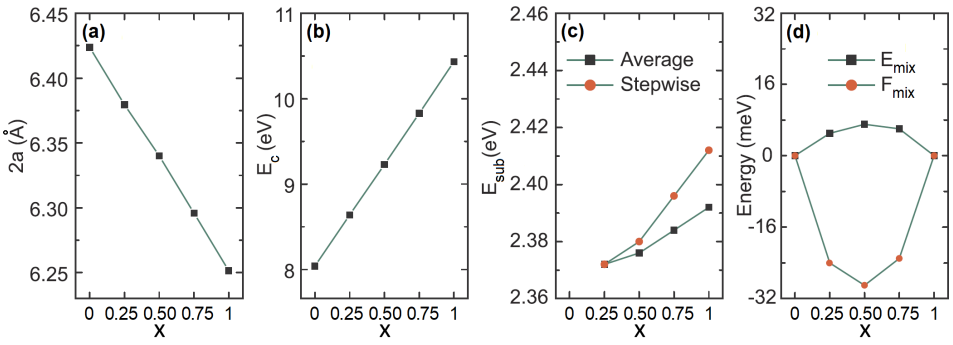

Figure 3.2: The variation of **(a)** Lattice constant, a **(b)** Cohesive energy, E_c **(c)** Substitution energy, E_{sub}), and **(d)** Mixing energy, E_{mix} with x.

shown in Fig. 3.2(c), the calculated average E_{sub} is positive for all x, implying that substitution is energetically favored. This result is correlated with the E_c of end-point pristine systems where E_c(AlN) is significantly larger than E_c(GaN). We also calculate step-wise E_{sub} in addition to average E_{sub} formulated in the Methodology part. For this case, the energy of consecutive systems are compared instead of only bare h-GaN and similar results are obtained. Even though E_{sub} is positive, it does not guarantee that substitution is spontaneous. In order to analyze the reaction path for substitution, NEB technique is performed, starting from adsorption cite of Al on h-GaN. In this method a number of images between initial and final stable configurations of the system are obtained by interpolation. Then a target elastic band function is constructed, which sums up the energies of all images. For even interpolation along the path, a penalty term and a spring constant are implemented. Finally this function is minimized to obtain a reaction path, where the energies belonging to the intermediate states can be used for energy barrier calculation. Our NEB results indicate that there is a small energy barrier (79 meV) for Al to substitute Ga. The details of NEB calculation performed for Al adsorption onto GaN monolayer to obtain alloy of $Ga_{0.75}Al_{0.25}N$ is shown are available as Fig. 3.3. These results indicate the possibility of forming $Ga_{1-x}Al_xN$ by substitution of Ga with Al atoms.

Finally, we calculate the free (F_{mix}) and internal energy of mixing (E_{mix}) for $Ga_{1-x}Al_xN$. Even $E_{mix}(x)$ is small but positive (up to 6 meV/cell), F_{mix} becomes negative once mixing entropy is taken into account as illustrated in Fig. 3.2(d).

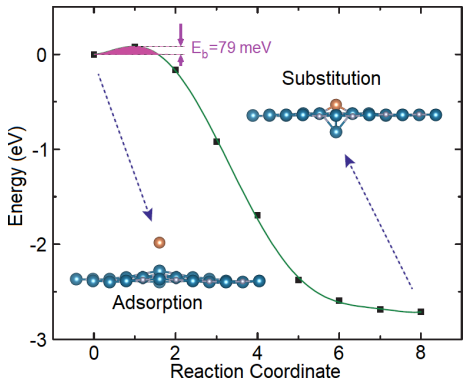

Figure 3.3: The reaction path for substitution of Ga atom Al calculated with Nudge Elastic Band approach. The initial and final positions are considered as adsorption and substitution sites of Al.

The entropic contributions promote mixing and the suggested alloys are thermodynamically stable without tendency of segregation at ambient temperatures. All the obtained results are summarized in Table 3.1.

Table 3.1: Optimized lattice constant a, bond length between cation and anion d_1(Ga-N) and d_2(Al-N), cohesive energy E_c (per pair), average substitution energy E_{sub}, Poisson's ratio ν, in-plane stiffness Y_{2D}, charge transfer from cation to anion Q*, indirect band gap E_{g-i} (HSE06 results are given in parenthesis) of $Ga_{1-x}Al_xN$ alloy.

	a (Å)	d_1 (Å)	d_2 (Å)	E_c (eV)	E_{sub} (eV)	ν -	Y_{2D} (N/m)	Q^* (e^-)	E_{g-i} (eV)
GaN	3.21	1.854	-	8.04	-	0.43	110	1.19	2.15 (3.42)
$Ga_{0.75}Al_{0.25}N$	3.19	1.853	1.807	8.64	2.371	0.44	110	1.32	2.41 (3.65)
$Ga_{0.50}Al_{0.50}N$	3.17	1.855	1.806	9.23	2.376	0.44	112	1.39	2.62 (3.81)
$Ga_{0.25}Al_{0.75}N$	3.15	1.853	1.807	9.83	2.382	0.45	112	1.46	2.78 (3.95)
AlN	3.13	-	1.805	10.43	2.390	0.46	114	1.59	2.91 (4.04)

3.3.2 Stability

Although negative F_{mix} at ambient temperature points out that alloy is energetically favored over segregated phases, we also analyze the dynamic stability of $Ga_{1-x}Al_xN$ systems. Firstly, we calculate the phonon frequency spectrum for all x. As shown in Fig. 3.4, all the phonon frequencies are positive, indicating that there are no imaginary modes in the spectrum and thus demonstrates the

stability of the considered structures. Additionally, gradual shift of optical modes with increasing x is noticed which can be correlated with the reduced total atomic mass and stronger bonds. To further test the stability against thermal excitation, which may cause the structure to dissociate emerging from the shallowness of its local minimum, we perform *ab initio* MD calculations on prototype $Ga_{0.5}Al_{0.5}N$ system. We start from 300 K and gradually increase the temperature to 600 K and finally 900 K for total simulation time of 3 ps. Apart from small fluctuations, the structure remains stable even at 900 K indicating a dynamic stability. MD results show that $Ga_{1-x}Al_xN$ alloy compositions are rather stable in their deep minimum on the Born-Oppenheimer surface and devices incorporating them can survive above room temperature. The snapshots of the atomic structure at different temperatures are given in Fig. 3.5.

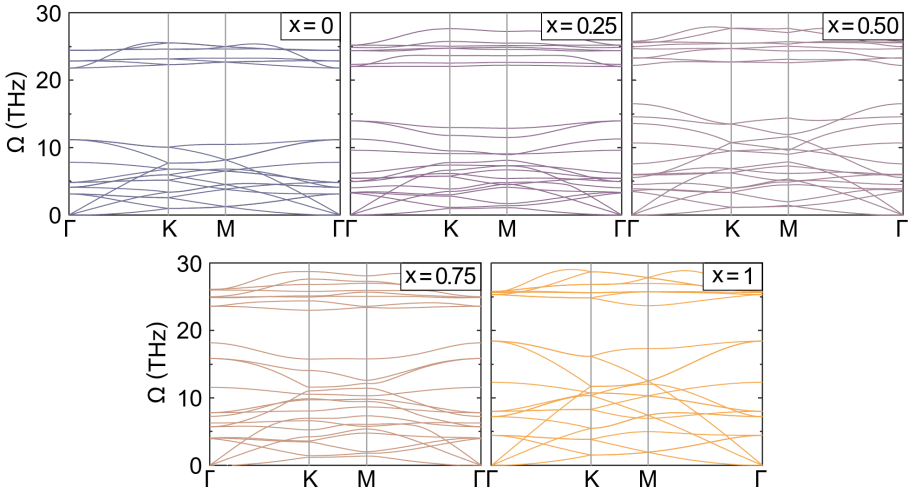

Figure 3.4: Phonon dispersion bands along major symmetry directions in the Brillouin zone calculated for $Ga_{1-x}Al_xN$ alloys. The 2×2 super cell (with respect to primitive unit cell of pristine system) is considered.

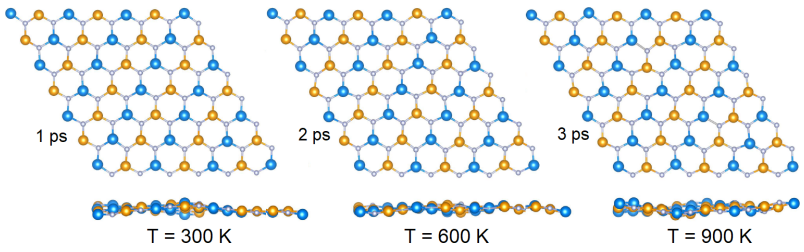

Figure 3.5: The snapshots of MD simulations of $Ga_{1-x}Al_xN$ at 300K, 600K, and 900 K. The total simulation time is 3 ps.

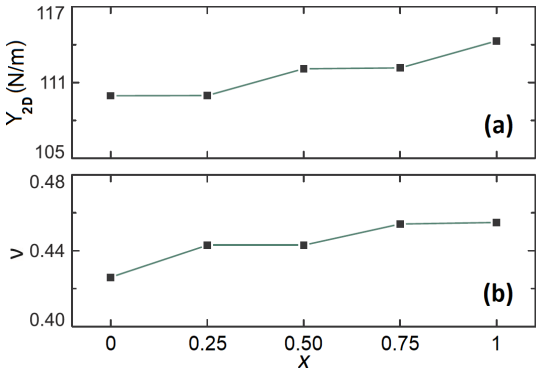

Figure 3.6: The variation of **(a)** in-plane stiffness (Y_{2D}) and **(b)** Poisson's ratio (ν) with x.

3.3.3 Mechanical properties

Resolving the atomic structure and stability, we analyze the fundamental properties starting from the mechanical response in the elastic regime. Strain engineering is a commonly used strategy to modify the physical properties of 2D systems [156, 157]. We calculate in-plane stiffness (Y_{2D}) and Poisson's ratio (ν) of considered systems by using the following formulas:

$$Y_{2D} = \frac{c_{11}^2 - c_{12}^2}{c_{11}} \quad \text{and} \quad \nu = \frac{c_{12}}{c_{11}} \tag{3.6}$$

where cij's are the elastic constants (hydrostatic and shear terms). The obtained values which are also listed in Table 1 for pristine h-GaN (Y_{2D}=110 N/m; ν =0.43) and h-AlN (Y_{2D} =114 N/m; ν =0.46) are in agreement with previous studies [113]. Both Y_{2D} and ν slightly escalates with increasing x as the endpoint values are close to each other and linear variation is not explicit [158] as shown in Fig. 3.6(a) and (b). When compared, Y_{2D} of $Ga_{1-x}Al_xN$ is significantly smaller than that of h-BN [159] (289±24 N/m) which is another member of 2D group III-nitrides, because of weakened Ga(Al)-N bond with respect to B-N bond (*i.e* $Ga_{1-x}Al_xN_1$ is softer). On the other hand ν is almost double times that of h-BN and also significantly larger than most of the realized 2D systems [157].

3.3.4 Electronic properties

Similar to their pristine constituents, $Ga_{1-x}Al_xN$ alloys are nonmagnetic, wide band gap semiconductors as shown in Fig. 3.7. The (indirect) fundamental band gap (E_{g-i}) arises from $\pi - \pi^*$ bands derived from antibonding-π and bonding-π bonds separated by a significant energy. The conduction band minimum (CBM) shifts to higher energy levels with increasing Al content, resulting in widening of E_{g-i}. This widening of E_{g-i} with x can be attributed the common-anion rule which anticipates an increase in band gap with decreasing atomic number, which in general holds for isovalent, common-cation (or anion) bulk semiconductors. Different from their bulk counterparts, $Ga_{1-x}Al_xN$ have indirect band gap between Γ-K points, ranging from 2.15 eV to 2.91 eV (calculated at DFT-PBE level) set by pristine systems. As expected, E_{g-i} blue-shifts once HSE06 correction is applied but the band profile and trends remained the same (Fig. 3.8). The dependence of E_{g-i} on x is nonlinear and deviates from Vegard's Law. The deviation from linearity can be quantified by a bowing parameter (β) which can be defined as:

$$E_g(Ga_{1-x}Al_xN) = xE_g(AlN) + (1-x)E_g(GaN) - \beta x(1-x) \tag{3.7}$$

and (β) is calculated as 0.35 eV. Albeit nonlinearity, evolution of band structure indicates that E_{g-i} can be adjusted continuously with varying x and thus tunable in the near UV range. In order to remove the possible constraints, the calculations at DFT-PBE level are repeated with 4×4 super cell and for different ordered configurations. Excluding the zone folding effects, similar electronic structure pattern is obtained and E_{g-i} only differs up to ±0.1 eV which confirms that size does not alter the obtained results [26,55].

Finally, work function of alloys (Φ_w) which describes the photoelectric threshold of the material are calculated. Φ_w is a critical parameter to control the field-emission properties of 2D optoelectronic devices. Φ_w(GaN) and Φ_w(AlN) are calculated as 4.41 and 4.40 eV, respectively, which are compatible with the earlier results [160]. In parallel with the obtained results for pristine systems, w of alloys remains almost constant (∼4.41 eV) and does not vary with the Al content.

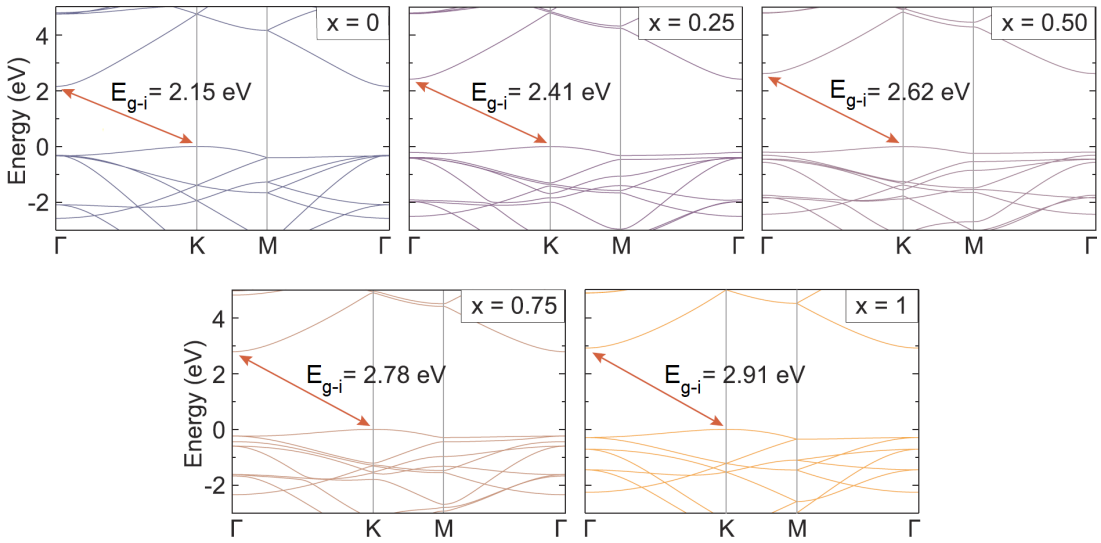

Figure 3.7: The electronic band structures of $Ga_{1-x}Al_xN$ for x = 0, 0.25, 0.50, 0.75, 1. The 2×2 super cell (with respect to primitive unit cell of pristine system) is considered. The fundamental band gaps are shown by red arrows. Fermi level is set to zero.

3.3.5 Thermal properties

Following the analysis of the phonon modes, we calculate the heat capacity (C_v) of the $Ga_{1-x}Al_xN$ as the contribution of lattice vibrations mainly dominates C_v at all practical temperatures. C_v determines not only the thermal energy stored within the alloy but also how quickly it radiates heat. C_v at constant volume can be calculated by [148]:

$$C_v = \sum_{q_j} k_B \left(\frac{\hbar\omega_{q_j}}{k_B T}\right)^2 \frac{\exp(\hbar\omega_{q_j}/k_B T)}{[\exp(\hbar\omega_{q_j}/k_B T - 1]^2} \tag{3.8}$$

where q is the wave vector, ω_{q_j} is the phonon frequency at q with phonon mode index j, T is the temperature, k_B is the Boltzmann constant and $\hbar$ is the reduced Planck constant. When compared, the variation of C_v(GaN) with T is compatible with earlier reports [161, 162]. As expected, C_v increases with temperature for all compositions and converges to a constant value of 24 $J.K^{-1}.mol^{-1}$ as shown in Fig. 3.9 approaching Dulong-Petit limit. At low T (*i.e* up to 300 K), C_v gets smaller values with increasing x. It can be correlated with the shift of optical

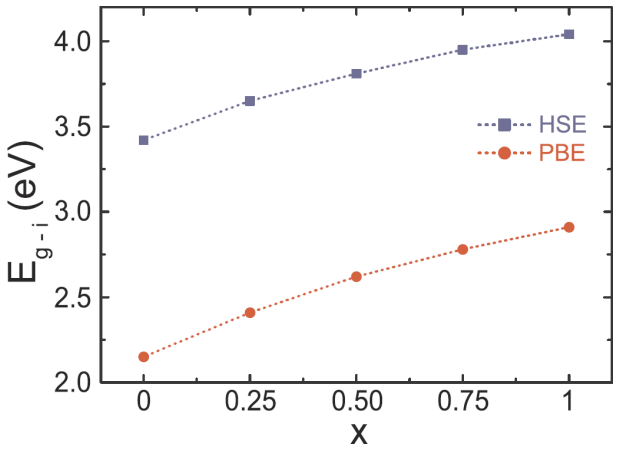

Figure 3.8: The variation of band gap (E_{g-i}) of $Ga_{1-x}Al_xN$ with x. E_{g-i} calculated with PBE and HSE06 are shown by red and blue lines, respectively.

modes with increasing Al content (Fig. 3.4) as C_v varies much faster for high-frequency optical phonon modes than low-frequency acoustic phonon modes at low temperature [161].

3.3.6 Optical properties

The optical response of $Ga_{1-x}Al_xN$ is analyzed by calculating the imaginary part of dielectric function ($\epsilon_2(\omega)$) which is presented in Fig. 3.10. The absorption onsets of $Ga_{1-x}Al_xN$ blue-shift with increasing x in compatible with the band gap of the structures. Main absorption peaks appear in the near UV region of the spectrum and they also shift to higher energy values as Al content increases. Moreover all systems have secondary remarkable absorption peak at far-UV region and their energies mainly depend on the constituent concentrations. The profile of $Ga_{0.75}Al_{0.25}N$ and $Ga_{0.25}Al_{0.75}N$ show similarity with the pristine h-GaN and h-AlN, respectively. While main peak of $Ga_{0.75}Al_{0.25}N$ ($Ga_{0.25}Al_{0.75}N$) blue-shifts, secondary absorption peak red-shifts when compared to h-GaN (h-AlN). In the case of $Ga_{0.5}Al_{0.5}N$ where Ga and Al contents are equal, two successive peaks for the main and secondary absorption are noticed indicating that the alloy possesses the character of both pristine systems equally. Due to the featured optical absorption over the UV range, alloys can be evaluated as a promising

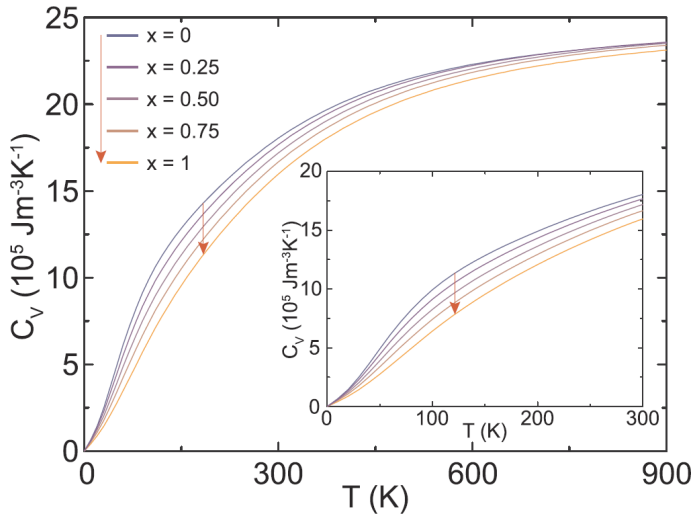

Figure 3.9: The variation of heat capacity (C_v) of $Ga_{1-x}Al_xN$ with temperature for different values of x. Low temperature behavior (up to room temperature) of C_v is given as an inset.

material for optoelectronic devices.

3.4 Conclusion

In summary, we design monolayer $Ga_{1-x}Al_xN$ ordered alloys with hexagonal lattice and investigate the variation of their structural, mechanical, electronic, thermal, and optical properties with concentration. We find that similar to pristine h-GaN and h-AlN, the planar geometry and hexagonal lattice are preserved. The optimized lattice constant gradually decreases with increasing x in accordance with Vegard's Law. The activation barrier to substitute Ga with Al is calculated to be low (79 meV) and moreover substitution is found to be energetically favorable. The mixing energy at ambient temperature is negative for all cases indicating that alloying is preferred against segregation. The phonon spectrum analysis and high temperature MD calculations further support the dynamical stability of the considered structures. The calculated in-plane stiffness indicates that $Ga_{1-x}Al_xN$ is softer than h-BN (or graphene) but has significantly high Poisson's ratio which is larger than most of the realized 2D systems. Similar to their

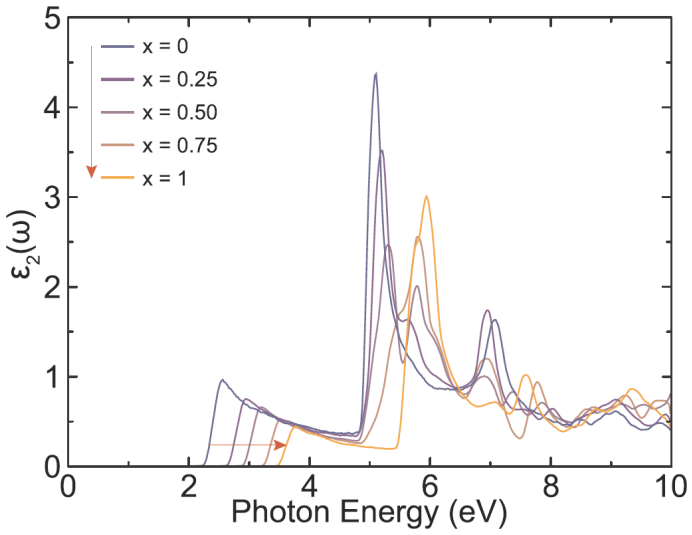

Figure 3.10: The variation of imaginary dielectric function ($\epsilon_2(\omega)$) of $Ga_{1-x}Al_xN$ with photon energy for different values of x.

pristine constituents, $Ga_{1-x}Al_xN$ alloys are wide, indirect band gap semiconductors. Band gap widens with increasing x (Fig. 3.11), albeit the variation is not linear. Heat capacity of the alloys has a tendency to decrease with increasing Al content at low temperatures but approaches the classical limit at high temperatures. The absorption onset of the considered systems remain in the near UV range and prominent absorption peaks blue-shifts with increasing x in compliance with the variation of the band gap. The stability of $Ga_{1-x}Al_xN$ ordered alloys and their continuously tunable fundamental properties suggest these systems as promising 2D semiconductors for wide range of applications at reduced scales.

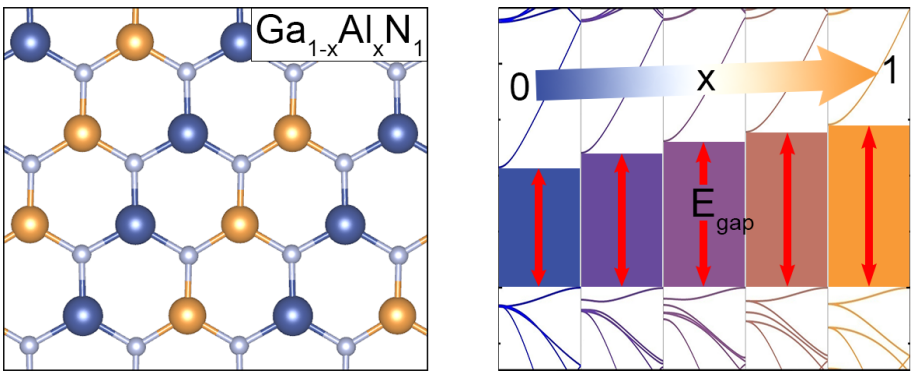

Figure 3.11: Electronic band gap opening with the increase of x in 2D $Ga_{1-x}Al_xN$ alloy.

Chapter 4

Alkali Batteries on Arsenene Monolayer

Part of this study is published as; M. Kanli, M.Kurban, B.Ozdemir, A.Onen, E. Durgun, Single- and multi-layer arsenene as an anode material for Li, Na, and K-ion battery applications, Computational Materials Science 186 (2021): 110000 [163].

4.1 Introduction

One of the emerging areas where pnictogens can find their potential applications is the field of rechargeable alkali-ion batteries, which are crucial for portable electronics and electric vehicle industry. Therefore, the interaction of alkali metals with 2D pnictogens has been a subject of various studies [60, 164–176]. In general, 2D structures supply much more accessible area than bulk materials for ion storage and diffusion, thus they are very attractive for battery applications. In this context, Li doped phosphorene has been studied and reported to have fast and directional diffusion, high average potential, and good electrical

conductivity [65]. Similar characteristics have been also predicted for Na intercalated phospherene [64]. Sun *et al.* have shown that a hybrid system composed of few-layer phosphorene sandwiched between graphene layers exhibits a high and reversible capacity of 2440 $mAhg^{-1}$ as a Na-ion battery electrode [73]. Accordingly, phospherene can offer higher capacities [64, 65] than graphene [177], MoS_2 [178], and Mo_2C [179], but without suitable dielectric capping. On the other hand, phosphorene has instability issues and is subject to degradation in ambient conditions [180]. Recently, antimonene has been revealed as an appealing anode material for Na-ion batteries as it enables recyclability, large-capacity (620 $mAhg^{-1}$), and fast electrochemical redox kinetics [62, 174]. Herein, 2D pnictogen sheets [73] provide rapid ion (de)intercalation and higher power densities when compared to graphene-based electrodes, which also suffer from clustering of alkali atoms [181].

However, arsenic has been less often investigated among pnictogens [182, 183]. Recently, Lim *et al.* [184] have synthesized arsenic and carbon nanocomposites and reported that this complex exhibits high reversible capacity in Li-ion (1306 $mAhg^{-1}$) and Na-ion batteries (750 $mAhg^{-1}$). Additionally, the interaction of alkali metals with SL buckled arsenene (SL-*hb*-As) phase has been investigated by *ab initio* methods and high storage capacities have been predicted [185]. The diffusion and voltage characteristics for Li-doped SL symmetric-washboard arsenene (SL-*sw*-As) have been also examined but for only at low concentration levels (below 20%) [186]. However, arsenene seems to be a potential anode material for alkali-ion batteries, wider concentration ranges and possible structural transformations should be explored including ML configurations of all the stable phases to reveal its full potential.

With this motivation, in this study, we investigate the interaction of alkali metals (M: Li, Na, and K) with SL and ML of arsenene phases (*hb*-As and *sw*-As). After obtaining the ground state structures, favorable adsorption sites of M adatoms and corresponding adsorption energies are determined. Next, the lateral diffusion and vertical intercalation barriers are calculated. Revealing the adatom adsorption, we examine alkali doped systems with varying concentrations (M_xAs, for $0 < x < 2$). *Ab initio* molecular dynamics calculations are

performed to check the stability of the doped structures and also to take into account the crystal-to-amorphous structural transformation at ambient conditions. Finally, average open-circuit potentials and specific capacities are calculated for ground-state configurations and their potential to be used in alkali-ion batteries are interpreted.

4.2 Method

Common references and parameters were given in Chapter 3.2 Method section.

The van der Waals (vdW) correction was included by using the DFT-D3 method with Becke-Johnson damping [187, 188]. A kinetic energy cutoff of 300 eV was taken for plane-wave basis set. The numerical integrations over the Brillouin zone were calculated by using Γ-centered 24×24×1 and 16×12×1 k-points meshes [149] for SL-*hb*-As and SL-*sw*-As unit cells, respectively and then scaled accordingly for larger cells and/or ML configurations.

The *ab initio* molecular dynamics (AIMD) calculations were performed at 300 K implying scaled velocity approach with 1 fs time steps up to 10 ps total simulation time. The average open-circuit voltage between two different concentrations can be calculated according to the following equation [173];

$$V_M = -\frac{G(M_{x_2}\mathrm{As}) - G(M_{x_1}\mathrm{As}) - (x_2 - x_1)G(M)}{q(x_2 - x_1)} \tag{4.1}$$

where $G(M_{x_1}As)$ and $G(M_{x_2}As)$ are the Gibbs free energies of M-doped arsenene with successive x_1 and x_2 alkali concentrations, $G(M)$ is the Gibbs free energy of bulk alkali metal, and q is the charge state of M (q=1). Gibbs free energy is approximated as the ground state energy since the contributions of pressure and entropy terms are not significant [189].

The specific (gravimetric) capacity is defined as;

$$C = \frac{nF}{3.6Z} \tag{4.2}$$

where n is the amount of the charge transfer between alkali and arsenic atoms (per mole), F is the Faraday constant, and Z is the atomic mass of arsenic (in g mol^{-1}). For theoretical capacity, the highest alkali concentration with stable configuration is considered.

The average binding energy is calculated as;

$$E_b = -\frac{E(M_x\text{As}) - E(\text{As}) - xE(M)}{x} \tag{4.3}$$

where $E(M_x\text{As})$ and $E(\text{As})$ are the ground state energies of alkali doped and pristine SL/ML arsenene phases, respectively. $E(M)$ is the energy of a single alkali metal atom, and x is the alkali concentration. The binding energy is also calculated with respect to total energy of bulk alkali metal and labeled as E_b'.

4.3 Results and discussione

4.3.1 Adatom adsorption and diffusion

We start with structural relaxation of SL-*hb*-As and SL-*sw*-As which are reported to be the stable phases of arsenene [51,57,58]. The optimized structures are shown in Fig. 4.1(a)-(b) The SL-*hb*-As has a hexagonal lattice similar to the layers of gray arsenic. The lattice constant ($a = b$) and As-As bond length (d_{As-As}) are calculated as 3.60 Å and 2.50 Å, respectively. On the other hand, the structure of SL-*sw*-As is similar to the layers black arsenic and has a rectangular lattice. a, b, and d_{As-As} are calculated as 3.69 Å, 4.76 Å, and 2.50 Å, respectively. The obtained structural parameters are consistent with the literature [58, 190]. It should be noted that while a transition from a symmetric to asymmetric phase is predicted for the washboard antimonene and bismuthene structures, such a transition is not noticed for arsenene [190].

Following the geometry optimization, we study the interaction of alkali metal adatoms with arsenene. The possible high-symmetry adsorption sites, namely,

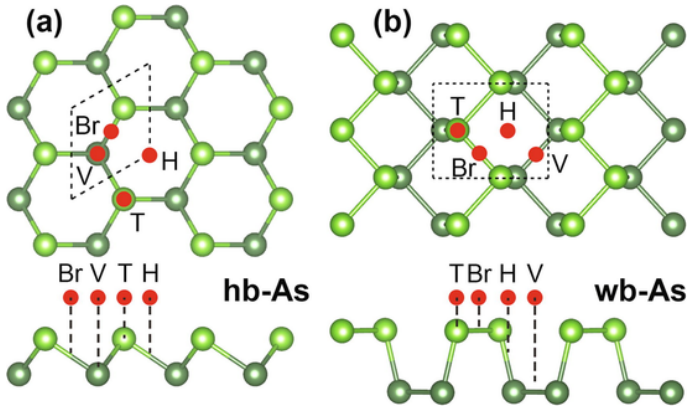

Figure 4.1: Structures of **(a)** SL-*hb*-As and **(b)** SL-*sw*-As. The high symmetry adsorption sites (Bridge (Br), Valley (V), Top (T), Hollow (H)) of alkali metal atoms are shown with red dots. (For interpretation of the references to color in this figure legend, the reader is referred to the web version of this article.)

Table 4.1: The adsorption energy with respect to a single alkali atom (E_a) or bulk alkali metal (E'_a) and corresponding bonding distance between alkali atom (M) and arsenene ($d_{\mathrm{As}-M}$) for high symmetry adsorption sites of SL-*hb*-As and SL-*sw*-As.

		Br			H			T			V		
Phase	M	E_a (eV)	E'_a (eV)	$d_{\mathrm{As}-M}$ (Å)	E_a (eV)	E'_a (eV)	$d_{\mathrm{As}-M}$ (Å)	E_a (eV)	E'_a (eV)	d_{As-M} (Å)	E_a (eV)	E'_a (eV)	$d_{\mathrm{As}-M}$ (Å)
hb-As	Li		$\rightarrow V$		1.54	-0.23	2.67	1.18	-0.59	2.45	1.62	-0.15	2.60
	Na		$\rightarrow V$		1.23	-0.01	2.99	0.98	-0.25	2.76	1.23	-0.01	2.97
	K		$\rightarrow V$		1.47	0.53	3.37	1.33	0.39	3.13	1.49	0.55	3.35
sw-As	Li	1.19	-0.34	2.54	1.81	0.28	2.50		$\rightarrow H$			$\rightarrow$ H	
	Na	0.97	-0.20	2.91	1.31	0.14	2.88		$\rightarrow H$		1.24	0.07	2.85
	K	1.32	0.41	3.24	1.58	0.67	3.25		$\rightarrow H$		1.53	0.62	3.21

hollow (H), top (T), valley (V), and bridge (Br), are shown in Fig. 4.1(a)-(b). Herein, 4×4 and 4×3 supercells are used for SL-*hb*-As and SL-*sw*-As, respectively, to minimize the $M-M$ interactions (d_{M-M} is ∼15 Å). The corresponding adsorption energies (E_a) and bond lengths (d_{As-M}) for each adsorption site are given in Table 4.1. For SL-*hb*-As, the most favorable adsorption site is the V-site with E_a of 1.62, 1.23, and 1.49 eV for Li, Na, and K, respectively. While H- and T-sites are also found to be local minima, M adatoms do not stay at Br-site and shift to V-site. On the other hand, for SL-*sw*-As, H-site is found to be the most stable adsorption site with E_a of 1.81, 1.31, and 1.58 eV for Li, Na, and K, respectively. Except Li atom, Br- and H-sites are also stable adsorption spots,

however adatoms initially on T-site move to H-site. When results are compared, E_a of SL-*sw*-As are slightly larger than those of SL-*hb*-As but being within the same range points out similar chemisorption characteristics. Positive E_a for all cases indicates that the adsorption is exothermic and M atoms favor the sites with maximum coordination number [64]. Considering the most favorable adsorption sites, Li has the strongest binding among Na and K. However, d_{As-M} follows the expected variation with the size of M, E_a does not regularly decrease down in alkali-group. This trend is correlated with the ionization energies of the M adatoms and their interactions with the substrate [172] clarifying Li > K > Na order. Bond strength of adatom over a substrate is an important parameter for battery applications [185, 186, 191–194]. Strong binding suggests that the migration of Li from the cathode to the anode should be more favorable than Na and K. This implies that the arsenene surfaces are more effective in attracting Li when compared to Na and K. Additionally, except Li, E_a' is positive for the most favorable sites indicating that alkali atom prefers to bind to arsenene instead of forming a cluster.

While calculated E_a (1.23-1.62 eV for SL-*hb*-As and 1.31-1.81 eV for SL-*sw*-As) are higher than those for graphene [171] (0.46-1.10 eV), they are within the same range but smaller than those for phosphorene [64, 65] (1.59-1.97 eV) and antimonene [61, 164, 174] (1.41-1.95 eV). Strong alkali-arsenene interaction can assure reversible battery operation and prevent alkali metal precipitation [191]. High adsorption ability of arsenene (especially for Li) can provide enhancement of cycling stability of battery and improve the performance of cathode.

The ion diffusion in the anode is one of the significant parameters during the charging and discharging process as it considerably influences the battery performance. Therefore, we calculate the energy barriers (ΔE) of M along possible diffusion pathways by using NEB technique and the results are shown in Fig. 4.2(a)-(b). Our results show that V - H - V and H - V - H are the fastest diffusion pathways for all M adatoms on SL-*hb*-As and SL-*wb*-As, respectively and ΔE(*hb*-As) is slightly smaller than ΔE(*sw*-As). For Li, ΔE are calculated as 0.11 eV and 0.12 eV, they are lower than that of black phosphorene (0.68 eV)

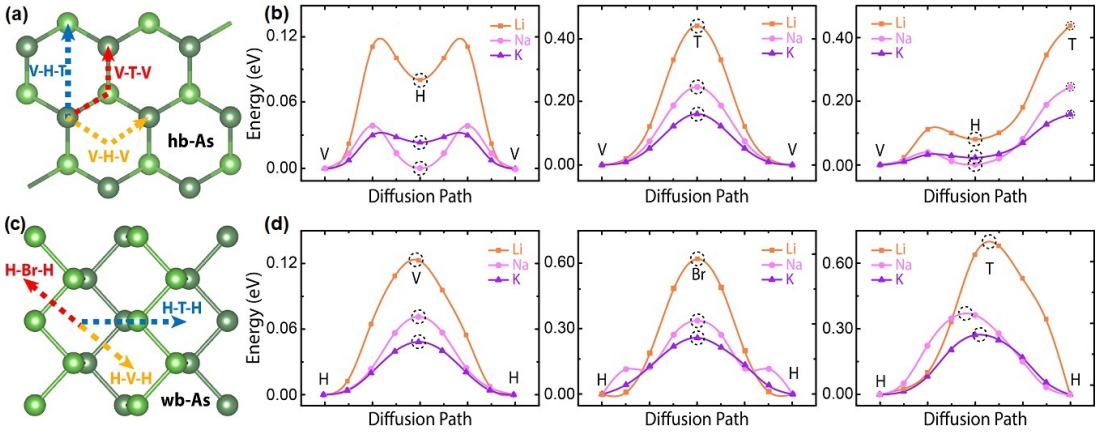

Figure 4.2: Lateral diffusion pathways and the energy variation for **(a)**,**(b)** SL-*hb*-As and **(c)**,**(d)** SL-*sw*-As.

along armchair direction [195], silicene (1.2 eV) [196], MoS_2 (0.25 eV) [197], VS_2 (0.22 eV) [197], graphene (0.33 eV) [198], germanene (0.5 eV) [196] and close to that of stanene (0.1 eV) [196]. On the other hand, they are higher than that of black phosphorene (0.08 eV) along zigzag direction [195]. For Na, ΔE are equal to 0.04 eV and 0.07 eV and are much smaller than that of silicene (3.56 eV), germanene (2.19 eV) and stanene (0.8 eV) [196]. Lastly, for K, ΔE are obtained as 0.03 eV and 0.05 eV, and are smaller than that of C_3N monolayer (0.07 eV) [199] and blue phosphorene (0.05 eV) [200]. In general, ΔE decrease from Li to K, and they are smaller than the reported diffusion barriers for various 2D systems, indicating fast diffusivity, which is a notable feature to be considered as an anode material for alkali-ion batteries.

4.3.2 Alkali metal doping: single-layer

In this section, we investigate M doping of SL-*hb*-As and SL-*sw*-As for varying concentrations (M_xAs). For each case, various doping sites are tested and the lowest energy configurations are determined. The optimized structures are represented in Fig. 4.3(a)-(b). It is revealed that the crystalline structures are preserved up to M_2As and $M_{0.5}$As for SL-*hb*-As and SL-*sw*-As, respectively. It should be noted that the highest concentration for Li/Na is smaller than the

theoretical expectation [184] as only the ordered patterns are taken into consideration.

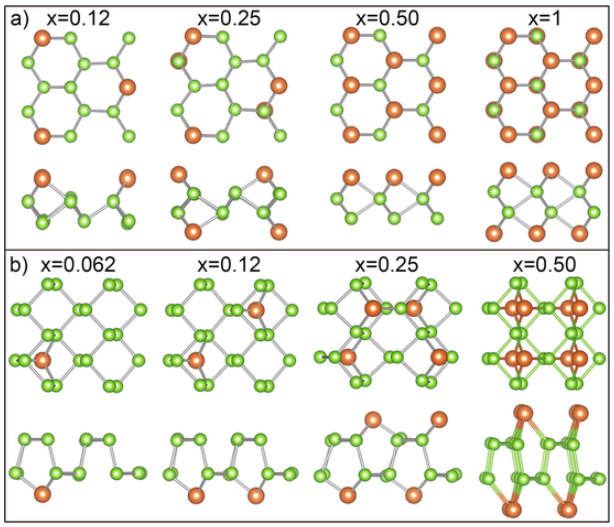

Figure 4.3: The optimized structures of M-doped (a) SL-*hb*-As and (b) SL-*sw*-As, for varying M concentrations (M_xAs).

The average binding energies of alkali metals, $E_b(M)$ for varying x are summarized in Table 4.2. E_b(Li, Na, K) are calculated to be in the range of 1.57-1.76 eV, 1.10-1.27 eV, and 1.05-1.20 eV for SL-*hb*-As. Similar to E_a, they are smaller

than those for SL-*sw*-As, which are calculated as 1.90-1.98 eV, 1.40-1.52 eV, and 1.42-1.66 eV. For SL-*hb*-As, however, E_b(Li,Na) are smaller than the corresponding E_a(Li,Na) up to x=0.5, they surpass it above this concentration. On the other hand, $E_b(K)$ is smaller than E_a(K) for all concentrations. For SL-*sw*-As, $E_b(M)$ is (in general) larger than $E_a(M)$. However, there seems like an increase in average binding energy, this is actually can be attributed to the energy lowering due to structural deformations (see below). Positive E_b' for all cases confirms that alkali atoms favor bonding to arsenene instead of cluster formation. Together with $E_b(M)$, the formation energy of M_xAs ($E_f(M)$) is calculated. For both phases, $E_f(M)$ are smaller than those of bare arsenene (3.13 eV) [190] for all M_xAs and they also decrease with increasing x. The decrease in $E_f(M)$ is due to the weakened electrostatic interaction between arsenene and M atoms and enhanced $M-M$ repulsion in ordered configurations.

It should also be noted that while pristine arsenene phases are semiconducting, alkali-doped systems are metallic, as observed previously [185, 186]. As shown in the corresponding electronic band structures for $x = 0.5$ (Fig. 4.4), band crossings occur with Fermi level and alkali doping converted the pristine structures into metallic character. Dirac cones can be observed especially for *hb*-As, as seen in graphene.

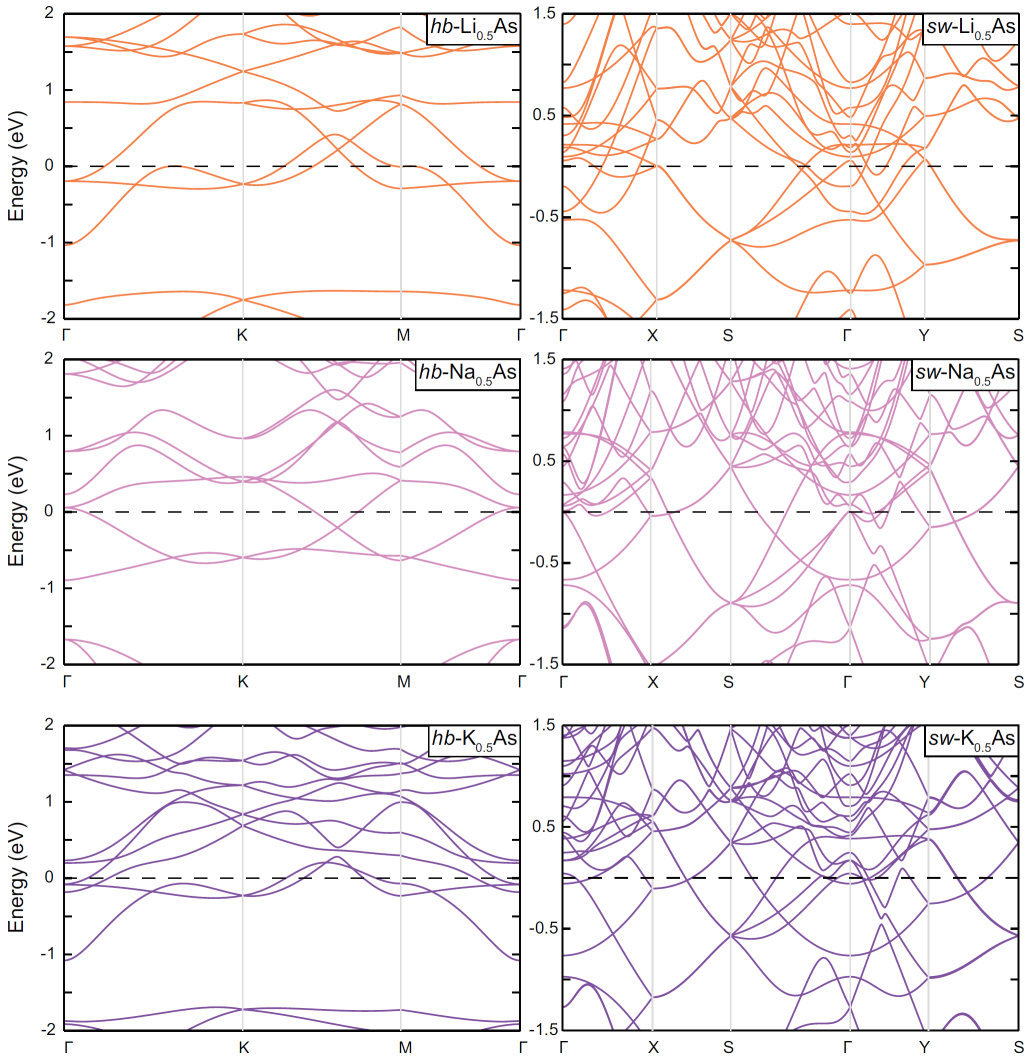

Figure 4.4: The electronic band structures of $M_{0.5}$As configurations of hexagonal buckled (hb) and symmetric washboard (sw) phases.

Open-circuit voltage (V_M) with respect to M is an important parameter which characterizes the performance of the alkali-ion battery and shows the capacity of an anode. Assuming a standard half-cell reaction, a theoretical V_M profile can be

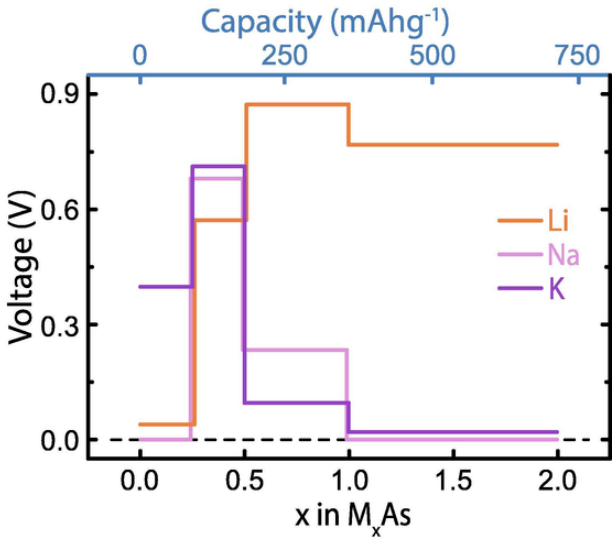

Figure 4.5: Average open-circuit voltages for SL-*hb*-As coated with alkali metals (Li, Na, and K) with varying concentration (M_xAs). The optimized (amorphous) structures are obtained with *ab initio* molecular dynamics calculations performed at ambient temperature.

estimated as an average voltage by using Equ. 4.1. V_M has been reported for alkali doped arsenene phases presuming that the crystalline structure is maintained at ambient conditions [185,186]. Although we also start with ordered configurations, deformations are noticed with increasing x, indicating a probable crystalline to amorphous transition. To reveal this issue, we perform AIMD calculations at 300 K up to 10 ps for SL-*hb*-As. This phase is considered as a prototype since its storage capacity is higher than that of SL-*sw*-As. Following the AIMD steps, the total energy of the system is significantly lowered, the crystallinity is altered, and an amorphous-like (unordered) structure is obtained. The revised V_M with respect to the total energy of amorphous structures for varying x and also for specific capacity (C) is shown in Fig. 4.6. However, the calculated V_M values are lower than the estimated data for crystalline phases, they are comparable with the experimental results [184]. The $V(M)$ reach up to a maximum of 0.88, 0.68, and 0.72 V for Li, Na, and K, respectively, and follow a sequence of $V_{Li} > V_{Na} > V_K$. The variation of voltage depends not only on the M type but also on the anode material. For instance, the trends in graphite and boron doped graphite (BC_3) are $V_K > V_{Li}$ (Na does not even intercalate graphite) [201] and $V_K > V_{Na} > V_{Li}$ [202], respectively. Moreover, the experimental voltage order of bulk arsenic

[184] is measured as $V_{Li} > V_{Na}$, which agrees with our results. Different from crystalline phases, V_M rise up to $x = 1$ for Li, and $x = 0.5$ for Na and K and then starts to decrease for increasing cation content. This could be due to the fact that amorphous phase becomes more stable with doping up to a certain concentration. The $V_{Na,K}$ reduces almost to 0 V for x >1, indicating that the suggested configuration cannot occupy that amount of alkali metals. The obtained V_M are lower than Li (and Na) doped antimonene (1.22 V) [174], phosphorene (2.9 V) [65], graphite (∼1.5 V) [197], TiO_2 (∼1.5 V) [203], 2H-MoS_2 (1.25 V) [204] and 1H-VS_2 (1.30 V). It should be noted that the desired potential range is between 0.1-1 V for anode materials [205]. Additionally, the corresponding (maximum) theoretical specific capacity (C) is 715 mAhg^{-1} and 358 mAhg^{-1} for Li and Na/K, respectively. Thus, M_xAs with a high C can be a promising candidate for low charging voltage applications.

4.3.3 Alkali metal doping: multi-layer

Next, we study the M-doped multilayer (periodic) arsenene phases (ML-*hb*-As and ML-*sw*-As) for varying concentrations (M_xAs). We start by analyzing Li intercalation through arsenene layers. Li has chosen as an exemplary, since it has the smallest radius and the calculated energy barriers (ΔE) can set the lowest limit. The intercalation paths and the energy variation are shown in Fig. 4.7. ΔE are calculated as 1.50 and 0.87 eV for ML-*hb*-As and ML-*sw*-As, respectively. Even ΔE for ML-*sw*-As is significantly smaller than that of ML-*hb*-As, it is still very high for room temperature diffusion, indicating the difficulty of intercalating M atoms. Accordingly, the intercalation (also leakage) can only occur through the vacancies or edges of the material.

The optimized structures of M_xAs for both phases are shown in Fig. 4.8. The ordered configurations are obtained up to $x = 1$ for ML-*hb*-As, and $x = 0.25$ for *sw*-As. M atoms are initially placed on V- and H-sites, which are found to be the most favorable adsorption sites for SL cases. The corresponding $E_b(M)$ and E_f energies are given in Table 4.3. $E_b(M)$ are higher than those for SL cases and

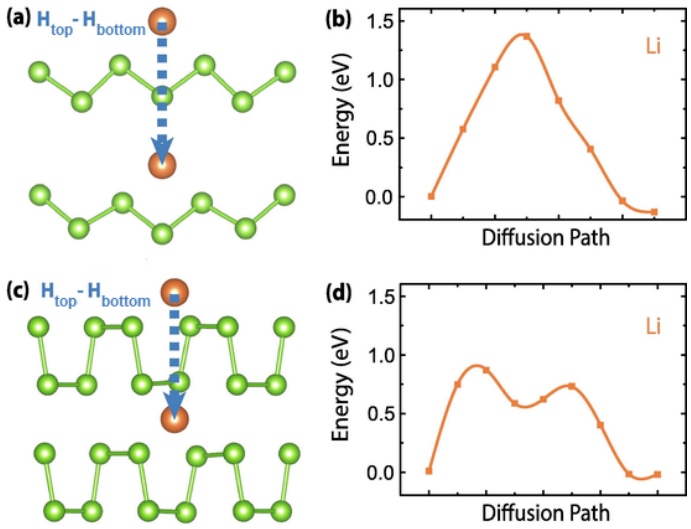

Figure 4.6: Vertical diffusion pathways and the energy variation for intercalation of Li in (a)-(b) ML-*hb*-As and (c)-(d) ML-*sw*-As.

also E_a, but follow a similar trend. The increase in $E_b(M)$ is partly due to the structural deformation as discussed above. Similar to SL case, E_f decrease with increasing x and they are smaller than those of pristine arsenene phases (3.29 eV) for all the concentrations. Variation of E_f implies that ML-M_xAs is becoming less stable with increasing cation content. It should be noted that, once the ordered pattern constrained is imposed, C decreases in ML-M_xAs when compared to SL configurations.

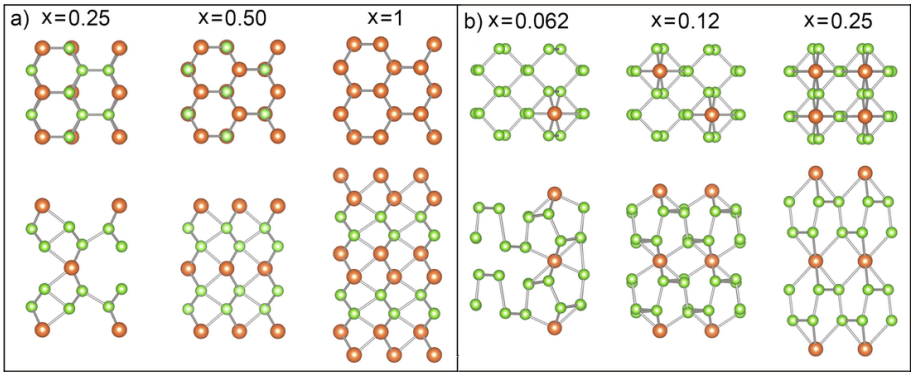

Figure 4.7: The optimized structures of M-doped (a) ML-*hb*-As and (b) ML-*sw*-As, for varying M concentrations (M_xAs).

Prior to estimation of V_M, AIMD calculations are performed for ML-*hb*-As to obtain lower energy configurations. Similar to SL cases, crystalline to amorphous

phase transition is noticed at ambient temperature. V_M, which are calculated with respect to the lower energy configurations, are shown in Fig. 4.9.

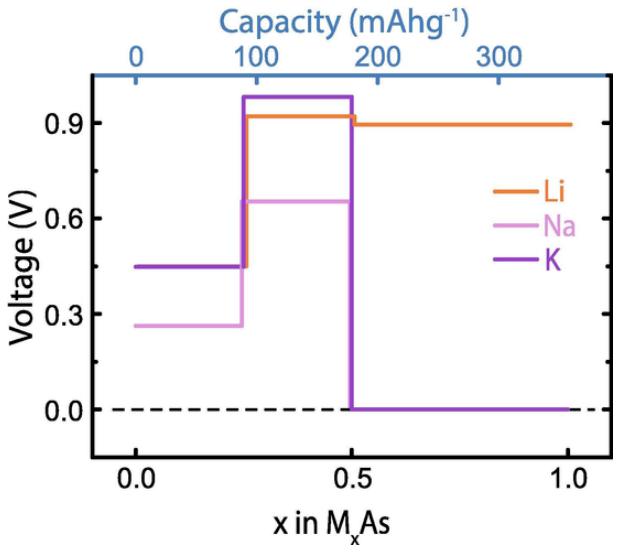

Figure 4.8: Average open circuit voltages for ML-*hb*-As coated with alkali metals (Li, Na, and K) for varying concentration (M_xAs). The optimized (amorphous) structures are obtained with *ab initio* molecular dynamics calculations performed at ambient temperature.

The maximum of V_M is calculated as 0.92, 0.65, and 0.98 V for Li, Na, and K, respectively, reaching C=358 mAhg^{-1} and the obtained results are comparable with the experimental data [184]. The V_M increase up to x=0.5 and then start to decrease and follow a similar trend to the SL cases. For ML-M_xAs, while V_M is higher than that of SL-M_xAs, C falls by half but still suitable for low charging voltage applications.

4.4 Conclusion

In summary (Fig. 4.10), we performed first-principles calculations to reveal the interaction of alkali metal atoms (M: Li, Na, and K) with SL and ML (periodic) structures of *hb*-As and *sw*-As phases. Adatom adsorption analyses imply that M-atoms strongly bind to arsenene surface with adsorption energy range of 1.3-1.8 eV. The strong adatom-electrode binding suggests that the migration of ions from

the cathode to the anode should be more favorable, thus it helps to alleviate the shuttle effect and enhance the cycling stability of the battery. The lateral diffusion energy barriers on arsenene are calculated to be low with the order of Li>Na>K and indicate fast diffusion for all ions. The structures are doped with varying M-concentration (M_xAs) and ordered patterns are obtained up to $x = 2$ for SL and $x = 1$ for ML systems. The theoretical storage capacity of *hb*-As is found to be higher than that of *sw*-As. On the other hand, deviations in ordered pattern and the decrease in formation energy with increasing doping level point out a possible structural transformation. The AIMD calculations indeed reveal that crystalline to amorphous phase transition occurs even for low concentrations level at ambient temperature. The corresponding (average) open-circuit voltages are found to be 0.68-0.88 V (0.65-0.98 V) with specific capacity up to 715 mAhg^{-1} (358 mAhg^{-1}) for SL (ML) configurations. Overall, non-crystalline phases are energetically more favorable than crystalline configurations and they provide more coherent results when compared with experimental data. The obtained voltage profile together with low diffusion barriers and strong metal-electrode binding suggests arsenene as a promising anode material to be used in for alkali-ion battery applications.

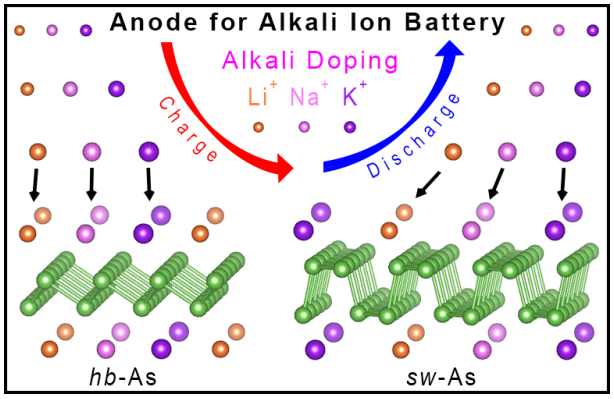

Figure 4.9: Alkali metal ion-anode interaction in rechargeable battery using *hb*- or *sw*-arsenene as its anode material.

Table 4.2: The average binding energies calculated with respect to single alkali atom (E_b) or bulk alkali metal (E_b') and the average bonding distance between alkali atom and arsenene ($d_{\mathrm{As}-M}$) for SL-*hb*-As and SL-*sw*-As with varying M concentrations (M_xAs).

Phase	M	x	E_b (eV)	E_b' (eV)	E_f (eV)	$d_{\mathrm{As}-M}$ (Å)
hb-As	Li	0.12	1.58	0.00	2.98	2.57
		0.25	1.61	0.02	2.84	2.55
		0.50	1.57	-0.01	2.62	2.60
		1.00	1.76	0.17	2.45	2.60
		2.00	1.73	0.14	2.20	2.69
	Na	0.12	1.10	0.03	2.92	2.93
		0.25	1.10	0.04	2.74	2.95
		0.50	1.21	0.15	2.50	3.32
		1.00	1.27	0.20	2.21	3.17
		2.00	1.29	0.22	1.91	3.07
	K	0.12	1.20	0.38	2.93	3.27
		0.25	1.15	0.33	2.75	3.31
		0.50	1.05	0.23	2.45	3.36
		1.00	1.15	0.32	2.15	3.42
		2.00	1.07	0.25	1.76	3.47
sw-As	Li	0.062	1.93	0.33	3.11	2.50
		0.12	1.97	0.37	3.05	2.50
		0.25	1.95	0.34	2.93	2.46
		0.50	1.97	0.37	2.78	2.52
	Na	0.062	1.42	0.34	3.08	2.87
		0.12	1.51	0.42	2.99	2.86
		0.25	1.44	0.35	2.83	2.88
		0.50	1.51	0.42	2.62	2.98
	K	0.062	1.64	0.77	3.09	3.21
		0.12	1.65	0.78	3.01	3.20
		0.25	1.54	0.67	2.85	3.22
		0.50	1.41	0.54	2.59	3.30

Table 4.3: The average binding energies calculated with respect to single alkali atom (E_b) or bulk alkali metal (E_b') and the average bonding distance between alkali atom (M) and arsenene ($d_{\mathrm{As}-M}$) for ML-*hb*-As and ML-*sw*-As with varying M concentrations (M_xAs).

Phase	M	x	E_b (eV)	E_b' (eV)	E_f (eV)	$d_{\mathrm{As}-X}$ (Å)
hb-As	Li	0.25	2.14	0.36	3.06	2.75
		0.50	2.34	0.57	2.90	2.75
		1.00	2.01	0.23	2.65	2.60
	Na	0.25	1.54	0.31	2.94	3.06
		0.50	1.73	0.50	2.77	3.05
		1.00	1.46	0.22	2.38	3.09
	K	0.25	1.41	0.46	2.92	3.35
		0.50	1.60	0.66	2.73	3.50
		1.00	1.10	0.16	2.20	3.48
sw-As	Li	0.062	2.29	0.69	3.30	2.47
		0.12	2.44	0.84	3.26	2.52
		0.25	2.58	0.98	3.21	2.57
	Na	0.062	1.13	0.04	3.23	2.73
		0.12	1.59	0.50	3.16	2.90
		0.25	1.84	0.76	3.06	2.97
	K	0.062	1.41	-0.69	3.17	3.06
		0.12	1.33	0.46	3.13	3.30
		0.25	1.68	0.81	3.02	3.34

Chapter 5

Dumbbell Phase Formation on hexagonal GaN Monolayers

5.1 Introduction

Extensive technological applications of group III-nitrides motivated many experimental and computational scientists to study functionalization of monolayer forms of these materials. To explore their intrinsic properties alloying, vacancy forming, doping and straining have been widely studied [9,10,82,84,88,89]. In this respect, adsorption is intensively researched, where alkalis, transition metals and group III to VII adatoms [206] were used to form structures having modified properties. Dumbbell (DB) formation has been observed on these structures [81,90–92]. This interesting geometry has been studied in detail for group IV monolayers [93, 95], where stable new phases of silicene and germanene are produced with diverse electronic and magnetic properties. They proposed graphitic Si or Ge multilayer synthesis by stacking these DB-including monolayers on top of each other. Those structures are buckled and unary. As an important member of group III-nitride monolayers, GaN has been broadly studied in respect to vertical and lateral heterostructures, in-plane junctions, functionalizations through doping to explore their intrinsic properties [90, 117, 118]. In this chapter this monolayer which is

a binary system with planar geometry is investigated for DB formation. Any monolayer from this nitride family has not been studied before in this respect.

5.2 Method

Common references and parameters were given in Chapter 3.2 Method section. For interionic charge-transfer analysis, Bader method [207] is used to obtain the effective charges on atoms.

5.3 Formation of Dumbbell and Its Coverage on GaN monolayer

When Ga and N atoms are approached on the surface of hexagonal GaN monolayer, there are various places that they might adsorb on, namely Br (Bridge, center of atomic bonds), H (Hollow, center of hexagonal ring), T_{Ga} (top of Ga) and T_{N} (top of N) sites. After checking all these places, T_N site is the most favorable adsorption site for both Ga and N atoms. Ga adatom, if not exactly placed over T_{Ga} site approaches and is adsorbed on T_N site, while N adatom is adsorbed on T_N site whereever it is placed. Also, for Ga adatom T_{Ga} or T_N are energetically very similar, while for N adatoms T_N is more favorable site by 1 eV. Therefore Ga-Ga and N-N DBs are considered for further calculations in this study.

N-N DB formation steps are shown in Fig. 5.1a. When single, free N adatom is approached to GaN monolayer, a DB geometry forms spontaneously. The adatom moves closer the monolayer surface and makes a bridge bond with three underlying Ga atoms ($\mathrm{Ga}_{1,2,3}$). It then starts to push the N atom beneath and finally DB is formed. Two N atoms above and below, named D_1 and D_2 receive significant electronic charge from the three nearest Ga atoms of monolayer, and hence, each

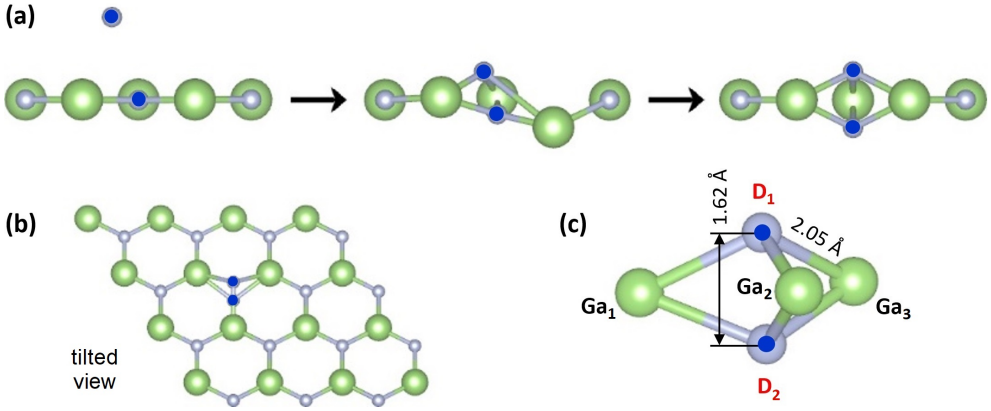

Figure 5.1: Snapshots of N-N DB formation over GaN monolayer. N adatom first approaches to the monolayer surface from the top site and eventually constructs the DB structure by pushing the host N atom down.

forms three strong N-Ga bonds with a length of 2.05 Å. Here, N-N DB corresponds to a crystal structure formed by two N atoms (D_1 and D_2) and three Ga atoms (lying in monolayer). More strongly bound $D_{1,2}$ atoms with a bond length of 1.62 Å have 3 + 1 coordination. Here $Ga_{1,2,3}$ atoms and the remaining N, Ga atoms of the monolayer have four-fold and three-fold coordination, respectively. Formation and bonding characteristics of DB geometry for our case come out to be very similar to Ge DB + germanene phase studied previously [93], except that for our case DB atoms have stronger bonds with each other than with the nearest-neighbour sites of the lattice.

For distinct DB coverages FDP (Full Dumbbell Phase), HDP (Hexagonal Dumbbell Phase), TDP (Trigonal Dumbbell Phase) and bigger unit cells (2x2, 3x3 and 4x4) are obtained, where Fig. 5.2 shows their atomic structures for Ga-Ga DBs. Exactly same layouts can be realized for N-N DB case. Similar three- and four-fold coordinations can be obtained for lower coverages (4×4, 3×3, 2×2, TDP) as indicated above for 3×3 case, while five- and six-fold coordinations can be observed in HDP and FDP phases, respectively. These numbers are valid for all of the phases with Ga-Ga or N-N DBs and can be checked from Fig. 5.2.

Convergence Tests: To obtain reliable results from *ab initio* calculations, both k-point set and cutoff energy should be tested carefully. Here HDP and

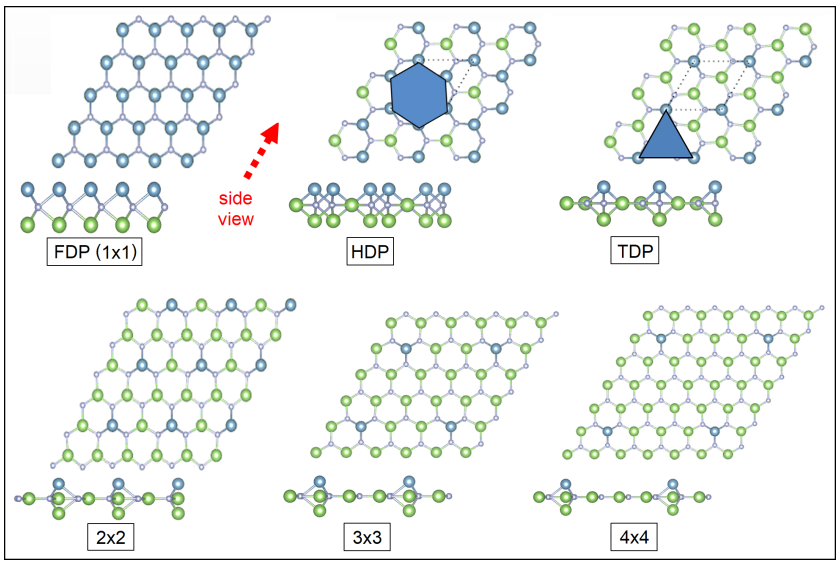

Figure 5.2: Atomic structures of various phases Ga-Ga DB + GaN monolayer, where periodically repeating unit cells can be formed for varying DB coverages over the monolayer surface.

TDP are chosen as representative phases to show these convergence tests. In Fig. 5.3(a,b) k-point and cutoff energy convergence test results can be seen. Accordingly the primitive unit cell is subdivided using a Γ-centered 12×12×1 mesh for the Brillouin zone integrations and the plane wave basis set is defined by an energy cutoff at 520 eV for all calculations. k-point sampling is adopted for electronic and phonon calculations. Also energetics for determination of their ground-state structure are given in Fig. 5.3(a).

5.4 Structure and Energetics

Table 5.1 gives structural, magnetic properties and energetics of Ga-Ga DB + GaN monolayer for a variety of unitcells having 2D hexagonal lattice structures (Fig. 5.2).

The binding energy for the formation of Ga-Ga/N-N DB is defined in terms of the total energies of DB + monolayer, pristine monolayer and single Ga/N adatom, in the following way: $E_b = E_T$[Ga/N] + E_T[GaN monolayer] - E_T[DB

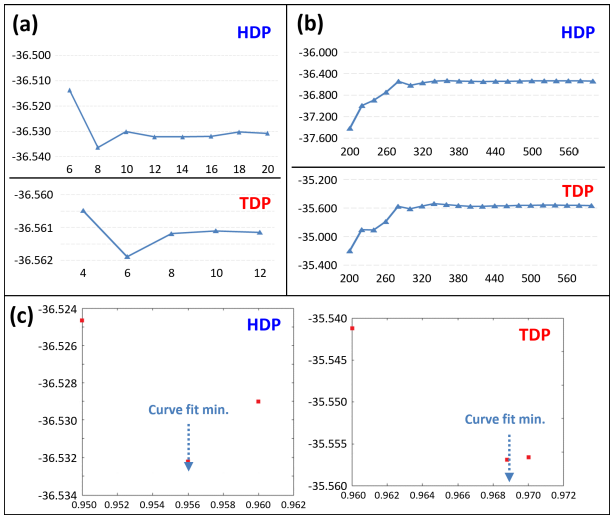

Figure 5.3: (a) Lattice constant calculation, The total energy variation as a function of b) k-points, (c) cutoff energy for Ga DB + GaN monolayer for HDP and TDP phases with 3x3 unitcell.

+ GaN monolayer]. E_b is calculated for a single DB in a set of hexagonal unit cells (1×1 to 5×5). Consequently it delivers the energy gained by a single DB formation by the adsorption of a single adatom to monolayer. Also $E_b > 0$ indicates an exothermic process. Very large unit cell is not considered here, since 5×5 unitcell gives a representative lattice space where DB-DB interaction can be ignored. The decreasing E_b values as the unitcells get smaller indicate repulsive interaction among DBs. The cohesive energy is defined as the difference between total energy of free atoms building the system and energy of the system per atom or simply the energy gained per atom by constructing a particular system. The associated E_c can be calculated with: $E_c = (n_{\mathrm{Ga}}\mathrm{E}_T[\mathrm{Ga}] + n_{\mathrm{N}}\mathrm{E}_T[\mathrm{N}]$ - $\mathrm{E}_T[\mathrm{DB}$ + GaN monolayer$])/n$, where E_T[Ga], E_T[N] and E_T[DB + GaN monolayer] correspond to total energies of single Ga, N atoms and DB + GaN monolayer. $n_{\mathrm{Ga/N}}$ and n indicate the number of single Ga/N atoms and total number of atoms in the unit cell, respectively.

We calculated the cohesive energy of the pristine GaN monolayer to be 3.96 eV, comparable with 4.02 eV of a previous study [9]. DB inclusion on unit cell results in a monotonic decreasing trend of cohesive energy, as shown for Ga-Ga DB in Fig. 5.4. N-N DB also gives a similar but softer trend. Comparing these E_c

Table 5.1: Calculated values for various phases of Ga-Ga or N-N DB + GaN monolayer, where n: number atoms in unit cell, d:bonding distance, $D_{1,2}$:DB atoms, E_b: Binding energy, E_c: Cohesive energy and : magnetic moment per unitcell.

Unitcell	Dumbbell		n	d (Å) Ga-N	d (Å) D_1-D_2	E_b (eV)	E_c (eV)	μ
1x1	Pristine		2	1.88	-	-	3.96	0.00
	Ga-Ga		3	2.19	2.62	1.11	3.01	0.46
	N-N			2.04	1.64	1.53	3.19	0.99
$\sqrt{3}$x$\sqrt{3}$	Ga-Ga	TDP	7	2.14	2.73	1.31	3.58	0.94
		HDP	8	2.19	2.66	1.00	3.22	1.35
2x2	Ga-Ga		9	2.29	2.73	1.27	3.66	1.00
	N-N			2.04	1.63	1.77	3.72	1.35
3x3	Ga-Ga		19	2.16	2.71	1.32	3.82	1.00
	N-N			2.03	1.62	1.73	3.85	1.00
4x4	Ga-Ga		33	2.16	2.71	1.34	3.88	1.00
	N-N			2.02	1.61	1.73	3.90	1.00
5x5	Ga-Ga		51	2.16	2.71	1.34	3.91	1.00
	N-N			2.08	1.61	1.73	3.92	1.00

values with that of pristine, DB geometry over GaN monolayer can be regarded as an unfavorable formation.

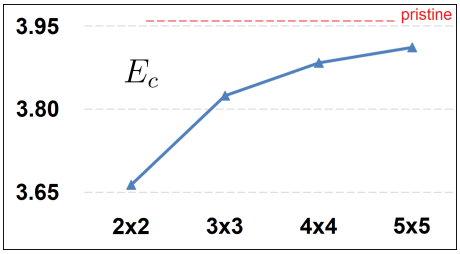

Figure 5.4: (a) Binding (E_b) and (b) cohesive (E_c) energy values (in eV) show a converging trend for decreasing the coverage of Ga-Ga DBs in GaN monolayer. Here unit cell change from 5x5 to 2x2 corresponds to an increase in DB coverage of the monolayer

This trend can be explained chemically by considering the concept of maximum coordination number. It is three for both Ga and N atoms, i.e. they form maximum three bonds with other atoms in their compounds or crystal structures. In pristine GaN monolayer, each constituting Ga or N atom has three neighbours which is same as their atomic maximum coordination number. As DB is formed,

Ga or N atom (to preserve the 2D layout) starts to have 4, 5 or 6 bonds depending on the degree of DB coverage. As can be inspected from Fig. 5.2, this number for Ga/N atom is 3/3, 3/4, 3/5 and 3/6 for pristine, TDP, HDP and FDP, respectively. So this concept seems to further explain the unfavorable energetics for Ga-Ga and N-N DB formations over GaN monolayer.

A more symmetrical DB placement helps TDP phase to have larger E_c values than HDP phase.

The reaction path for DB formation is analyzed by NEB technique, starting from adsorption cite of Ga on GaN. Our calculations indicate that there is a small energy barrier (80 meV) for Ga to form a Ga-Ga DB. The details can be seen in Fig. 5.5. These result indicates the possibility of Ga-Ga DB geometry by Ga adsorption on GaN monolayer.

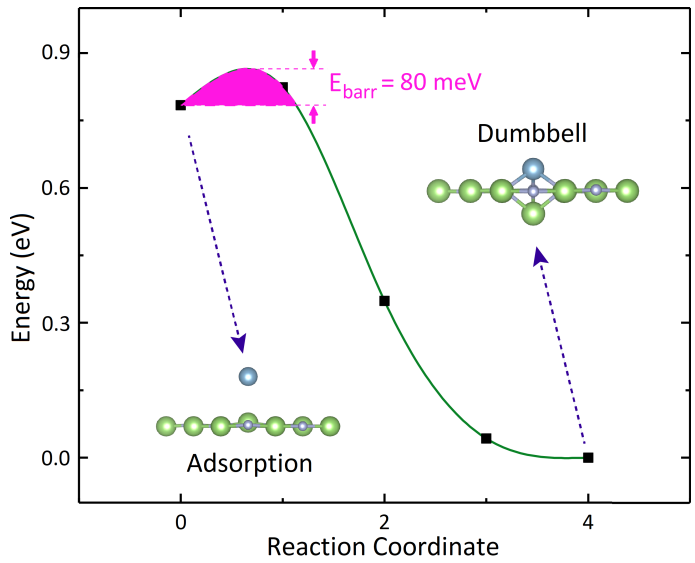

Figure 5.5: The reaction path for DB formation as Ga adatom is attracted to GaN monolayer, calculated with Nudge Elastic Band approach. The initial and final positions are considered as adsorption and DB sites of Ga.

This discussion has been made for similar DB structures formed on silicene monolayer by [94] and favorable DB formation is observed.

5.5 Stability of the Structure

Stability of free standing Ga-Ga DB + GaN monolayer structures is checked by applying atomic displacements, to calculate frequency of lattice vibrations and to specify phonon frequency spectra. *Ab initio* phonon dispersion curves include imaginary frequency modes for FDP, HDP and TDP phases, as can be seen in Fig. 5.6 and Fig. 5.7. Thus these high DB involving phases are prone to structural instability. MD calculations, giving many broken or newly generated bonds and having having structural distortion confirm this result further. FDP and HDP phases dissociates even after 1 ps of finite-temperature simulation from 0 to 300 K while TDP phase gets finite lattice distortions after 600 K. Opposite to these, phases with low DB coverages (2×2, 3×3 and 4×4) have stable structures, as can be seen in Fig. 5.8.

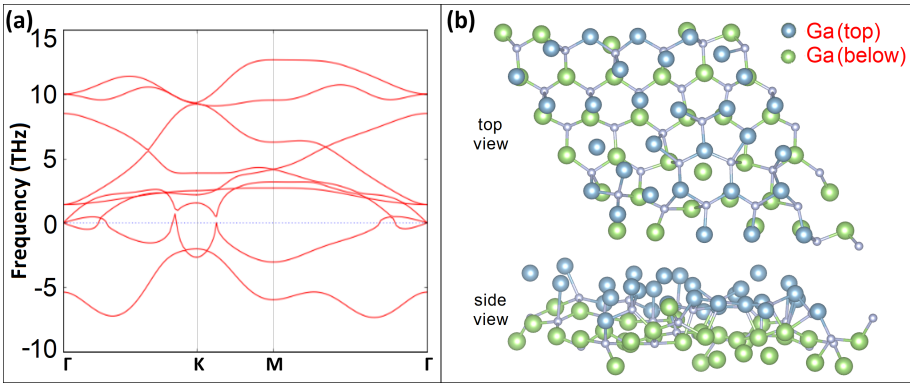

Figure 5.6: a) Phonon dispersion curves for Ga-Ga DB + GaN monolayer for 1x1 unitcell, b) Snapshots of atomic configurations at 1 ps (300 K), in which honeycomb-like structures are not maintained.

Opposite to these, phases with low DB coverages (2×2, 3×3 and 4×4) have stable structures, as can be seen in Fig. 5.8.

Stability of free standing N-N DB + GaN monolayer phase is only checked for 3x3 unit cell, which gives a stable structure as shown in Fig. 5.9.

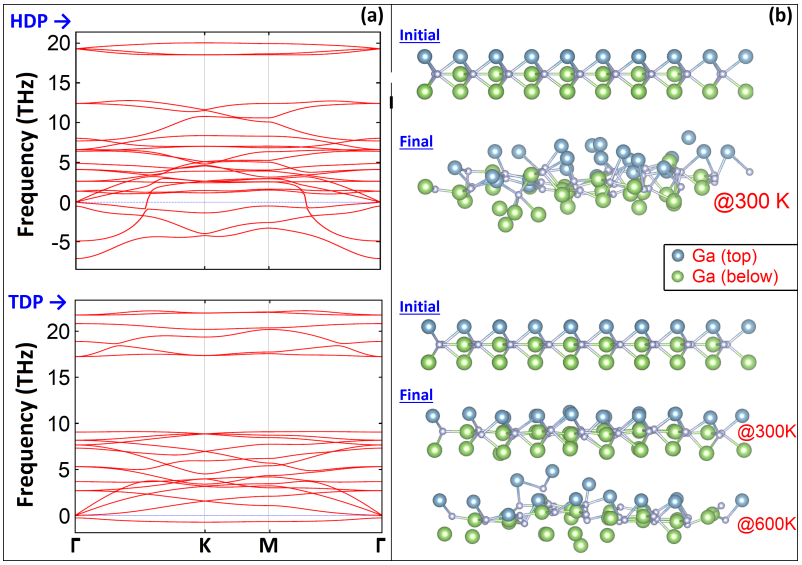

Figure 5.7: a) Phonon dispersion curves for Ga-Ga DB + GaN monolayer for HDP and TDP phases (3x3 unitcell), b) Snapshots of atomic configurations at 1 ps (300, 600 K), in which honeycomb-like structures are not maintained.

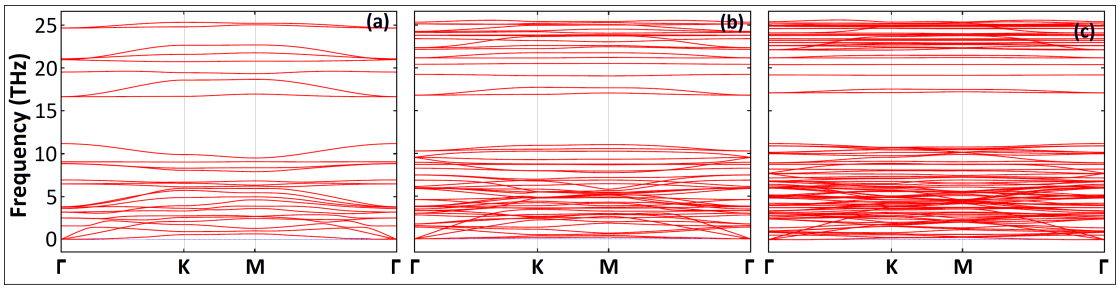

Figure 5.8: Phonon dispersion curves for Ga-Ga DB + GaN monolayer for (a) 2x2, (b) 3x3, (c) 4x4 unitcells.

5.6 Electronic Properties

As can be seen from the following bands, DB formation in general leads to spin-polarized impurity states. These are principally contributed by p-orbitals of the atoms in impurity zone (IZ) region. Here IZ is defined by two DB atoms and three nearest-neighbour atoms in the lattice, which can be observed from Fig. 5.1(c). In Ga-Ga/N-N DB geometries, Ga/N adatom pushes down host Ga/N atom. Thus both D_1 and D_2 atoms have sp^3-like hybridization where they have four-fold bonding with three nearest neighbour and one DB atoms.

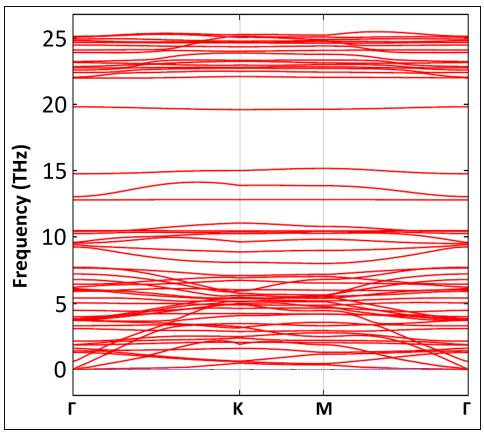

Figure 5.9: Phonon dispersion curves for N-N DB + GaN monolayer for 3x3 unitcell

For Ga-Ga DBs on 2×2, 3×3, 4×4 and 5×5 unitcells, electronic energy band structures are shown in Fig. 5.10. Ga dopant involves in bonding with its three valence electrons and the system shows a semiconductor character having four localized and spin-polarized bands contributed by IZ states. Here IZ states are mainly contributed by Ga s and N p orbitals.

For N-N DBs, energy bands of HDP, TDP, 2×2 and 3×3 phases are calculated as shown in Fig. 5.11. Here, five valence electrons of N dopant involve in bonding and the system shows metalic character. Here IZ states are mainly contributed by p orbitals.

With Bader analysis, interionic charge-transfers are calculated. As shown in Table 5.2, for Ga-Ga DB over 2×2, 3×3 and 4×4 unitcells very similar charge transfers are realized, namely each DB atoms (Ga) gives 0.69 electrons, Ga/N lattice atom donates/receives 1.37/1.37 electrons.

Table 5.2: Charges on atoms are calculated by using Bader charge analysis for Ga-Ga DB + GaN monolayer.

Charge on atoms (e)	Unitcell		
	2x2	3x3	4x4
Ga adatom	0.69	0.69	0.69
Ga (Monolayer)	1.34	1.37	1.37
N (Monolayer)	-1.36	-1.37	-1.37

In summary, pristine GaN monolayer having 2.15 eV band gaps becomes a metal upon N-N DB formation, while it preserves its semiconductor character but has a varying band gaps for different phases upon Ga-Ga DB formation.

5.7 Conclusion

To summarize, in this chapter we investigated the formation of DB structure upon adsorption of Ga, N adatoms to GaN monolayer using first-principles DFT methods. While Ga-N DB structures are not stably formed over the monolayer, Ga-Ga and N-N DB geometries are predicted in an exothermic and spontaneous scheme. Also, GaN monolayer can be periodically covered with each of both DB formations. However, comparing cohesive energies of the DB + GaN monolayer phases with that of pristine monolayer, these DB including geometries are unfavorable structures. For low coverage of DB, they show an band structure. For 2×2, 3×3, 4×4 and 5×5 phases, electronic energy band structures show spin-polarized and degenerate bands mainly contributed by p-orbitals of the atoms in impurity zone. Degenarated bands are not observed for N-N DB for HDP, TDP, 2×2 and 3×3 phases. Upon adsorption, semiconductor GaN monolayer become spin-polarized semiconductor with varying band gap. Functionalization of GaN monolayer with DB formation allows electronic structure to be tuned substantionally, which would be highly desired for nanoscale electronic and optical devices. These geometries may also be used for the synthesis of layered GaN structures.

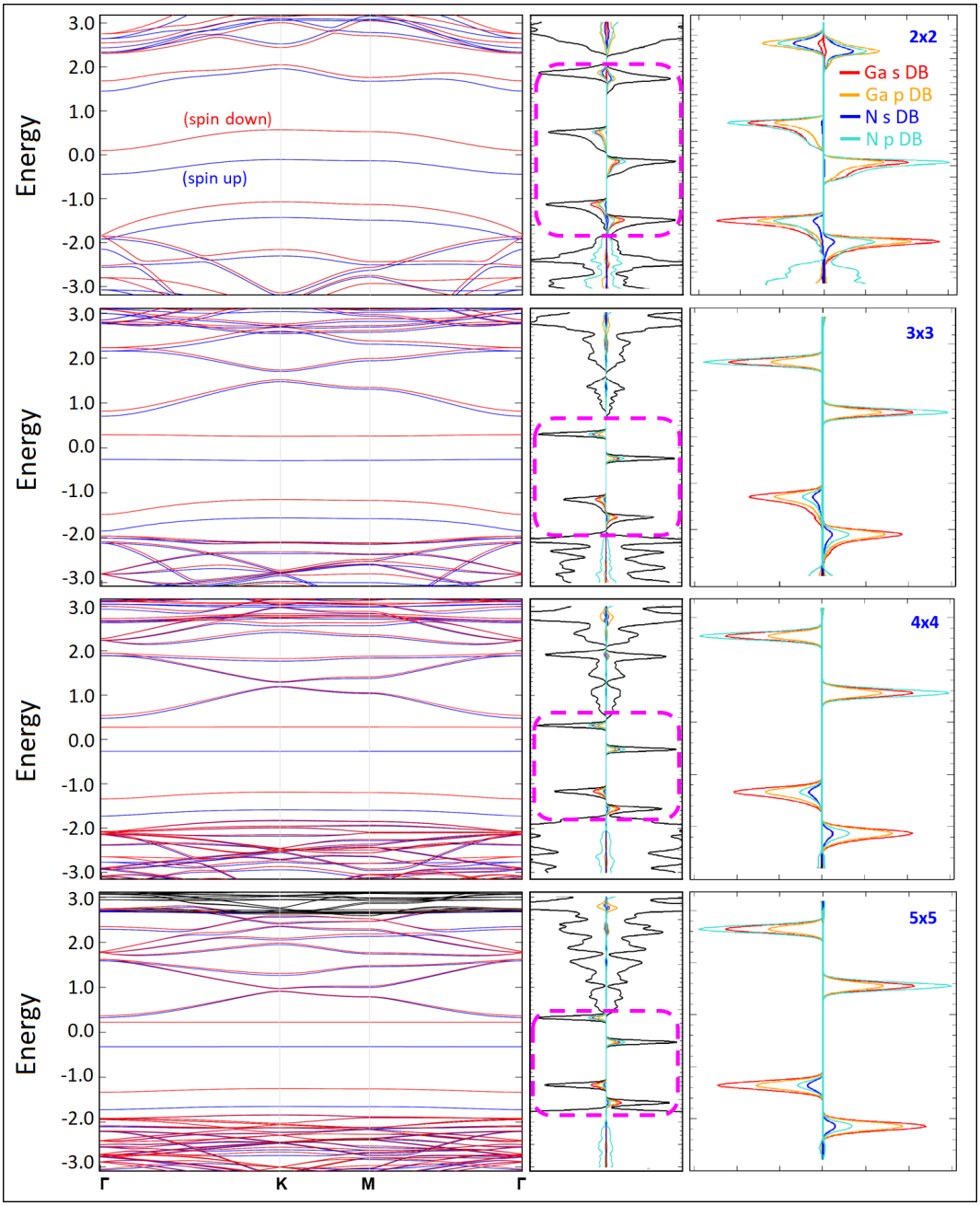

Figure 5.10: 1st column: Electronic band structure, 2nd and 3rd columns: partial density of states (PDOS) of impurity region and total density of states (DOS) of GaN upon DB formation for variety of DB coverages. Details of pink dashed rectangular region in 2nd column is shown in 3rd column)

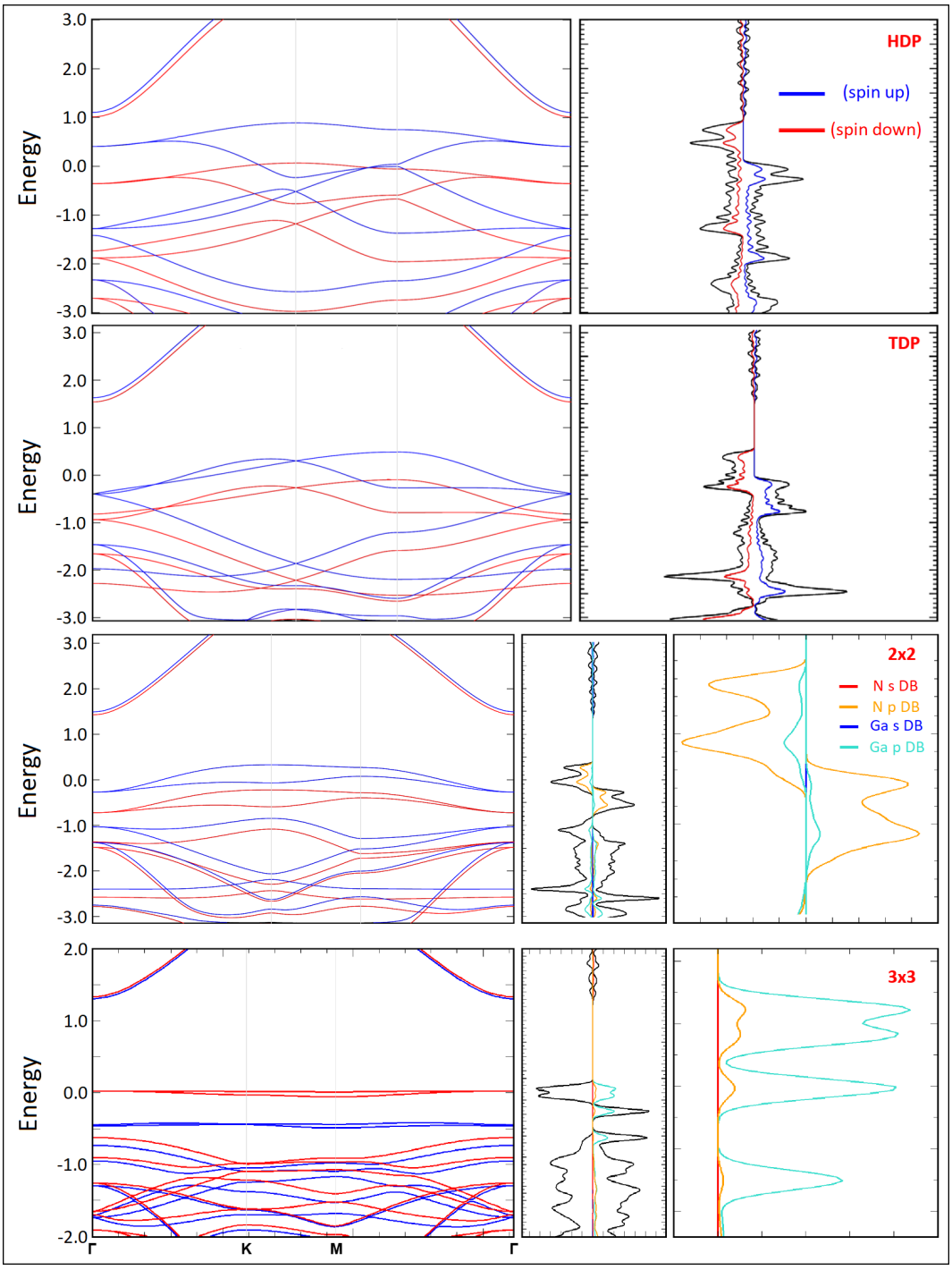

Figure 5.11: 1st column: Electronic band structure, 2nd and 3rd columns: partial density of states (PDOS) of impurity region and total density of states (DOS) of GaN upon DB formation for variety of DB coverages. For 3x3 and 3x3 unitcells (shown in 2nd and 3rd rows) details of pink dashed rectangular region in 2nd column is shown in 3rd column.

Chapter 6

Conclusions

This thesis was based upon the investigation of mechanical, electronic and optical properties of two-dimensional honeycomb-like materials. The primary aim was to understand the fundamental physical laws at nanoscale so as to use them in device designing. By *ab initio* studies new interesting properties were explored, a novel application for a conventinal material is offered and a novel functionalization method is explored.

In Chapter 3, where by alloying hexagonal GaN monolayer with Al atom, new ordered alloy forms of $Ga_{1-x}Al_xN$ for $x = 0, 0.25, 0.50, 0.75, 1$ were obtained. The electronegativity difference between Al and Ga produced a gradual increase in charge transferred to N with increasing x. Similar to lattice constant, cohesive energy of the alloy varies almost linearly with x but in an opposite trend. NEB method analysis for substitution of Ga with Al showed that using conventional chemical vapor deposition technique is feasible to produce such alloys. Via free energy and internal energy of mixing calculations, these alloys were found thermodynamically stable having no tendency of segregation at ambient temperature. Both phonon and MD analysis provided that all $Ga_{1-x}Al_xN$ alloys have stable structures. Gradual shift of optical modes with increasing x can be correlated with the reduced total atomic mass and stronger bonds. In stability tests against

thermal excitation on prototype $Ga_{0.5}Al_{0.5}N$ system, apart from small fluctuations the structure remained stable even at 900 K indicating a dynamic stability. Atomic structure snapshots at different temperatures indicate rather stable alloy structures, devices incorporating them can survive above room temperature. For mechanical response analysis in the elastic regime, both Y_{2D} and ν escalates slightly with increasing x as the endpoint values are close to each other, and does not show an explicit linear variation. Similar to their pristine constituents, $Ga_{1-x}Al_xN$ alloys are nonmagnetic, wide band gap semiconductors. E_{g-i} increases with x nonlinearly, deviating from Vegard's law with a bowing parameter of -0.35. The band gap is continously tunable in near UV range. When DFT-PBE calculations were repeated for 4×4 supercell for different ordered configurations with excluding zone folding effects, very minute differences of ±0.1 eV in E_{g-i} confirm that size does not alter the obtained results. Work function of alloys (Φ_w) remains almost constant (∼4.41 eV) for considered structures. The heat capacity C_v increases with temperature for all compositions and converges to the constant value of Dulong-Petit limit, as expected. Smaller values at low T with increasing x can be correlated with the shift of optical modes with increasing Al content. Concerning optical response, the absorption onsets of the alloys blue-shift with increasing x in compatible with their band gaps. Main absorption peaks appearing in the near UV region of the spectrum also shift to higher energy values as Al content increases. Moreover all systems have secondary remarkable absorption peak at far-UV region and their energies mainly depend on the constituent concentrations. The profile of $Ga_{0.75}Al_{0.25}N$ and $Ga_{0.25}Al_{0.75}N$ show similarity with the pristine h-GaN and h-AlN, respectively. While main peak of $Ga_{0.75}Al_{0.25}N$ ($Ga_{0.25}Al_{0.75}N$) blue-shifts, secondary absorption peak red-shifts when compared to h-GaN (h-AlN). In the case of $Ga_{0.5}Al_{0.5}N$ with equal atomic content, two successive peaks for the main and secondary absorption are noticed, indicating similar contribution from both pristine systems. The featured optical absorption over the UV range shows that the considered alloys can be a promising material for optoelectronic devices.

Alkali adsorption on arsenene monolayer was studied in Chapter 4. SL-*hb*-As and SL-*sw*-As stable phases of arsenene were obtained by structural relaxation.

Transition from a symmetric to asymmetric phase is not noticed for arsenene. Among possible high-symmetry adsorption sites, SL-*hb*-As has V-site and SL-*sw*-As has H-site as the most favorable adsorption site. Adsorption energy analysis for both phases demostrated that they have similar chemisorption characteristics, alkali adsorption is exothermic and M atoms favor the sites with maximum coordination number. In accordance with the ionization energies of the M adatoms, E_a decreases in Li > K > Na order. Binding strength analysis suggests Li migration from the cathode to the anode as being more favorable than Na and K. Additionally, except Li, E_a' is positive for the most favorable sites indicating that alkali atom prefers to bind to arsenene instead of forming a cluster. While the calculated E_a (1.23-1.62 eV for SL-*hb*-As and 1.31-1.81 eV for SL-*sw*-As) are higher than those for graphene (0.46-1.10 eV), they are within the same range but smaller than those for phosphorene (1.59-1.97 eV) and antimonene (1.41-1.95 eV). Strong alkali-arsenene interaction can assure reversible battery operation and prevent alkali metal precipitation. High adsorption ability of arsenene (especially for Li) can provide enhancement of cycling stability of battery and improve the performance of cathode. Ion diffusion in the anode is analyzed by NEB technique. V - H - V and H - V - H were obtained as the fastest diffusion pathways for all M adatoms on SL-*hb*-As and SL-*wb*-As, respectively. ΔE(*hb*-As) is slightly smaller than ΔE(*sw*-As). For both phases in general, ΔE decrease from Li to K, and they are smaller than the reported diffusion barriers for various 2D systems, indicating fast diffusivity, which is a notable feature to be considered as an anode material for alkali-ion batteries. For increasing alkali concentrations in M_xAs, preserved crystalline structures up to M_2As and $M_{0.5}$As were obtained for SL-*hb*-As and SL-*sw*-As, respectively. Here, the concern for ordered pattern limited the theoretical expectation. For both phases, formation energy are smaller than those of bare arsenene (3.13 eV) for all M_xAs and they also decrease with increasing x, which can be explained by the weakened electrostatic interaction between arsenene and M atoms and enhanced $M-M$ repulsion in ordered configurations. Regarding electronic structures, in contrast to the semiconductor pristine phases, alkali-doped systems were observed to be metallic. Dirac cones seen in graphene can be observed especially for *hb*-As. Average open-circuit voltage (V_M) is used to characterize the performance of the alkali-ion battery. Because of the noticed

deformations with increasing x, indicating a probable crystalline to amorphous transition AIMD calculations for SL-*hb*-As were performed. As a result the system had significantly lowered total energy and its crystallinity was altered, and an amorphous-like (unordered) structure was obtained. The calculated V_M values are lower than the estimated data for crystalline phases, but they are comparable with the experimental results. Reaching up to a maximum of 0.88, 0.68, and 0.72 V for Li, Na, and K, $V(M)$ followed a sequence of $V_{Li} > V_{Na} > V_K$. The variation of voltage depends not only on the M type but also on the anode material. Our results agreed with the experimental voltage order of bulk arsenic, measured as $V_{Li} > V_{Na}$. Different from crystalline phases, V_M rise up to $x = 1$ for Li, and $x = 0.5$ for Na and K and then starts to decrease for increasing cation content. This can be explained by the fact that amorphous phase becomes more stable with doping up to a certain concentration. The desired potential range is (0.1-1 V) and the corresponding theoretical specific capacity (C) (715 mAhg^{-1} for Li and 358 mAhg^{-1} for Na/K) provide M_xAs system with high C as a promising candidate for low charging voltage applications. For the study of M-doped multilayer arsenene phases for varying concentrations Li has been chosen as exemplary, since it has the smallest radius and the calculated energy barriers (ΔE) can set the lowest limit. Still very high ΔE even for room temperature diffusion indicate the difficulty of intercalating M atoms. Thus intercalation, also leakage can only occur through the vacancies or edges of the material. $E_b(M)$ are higher than those for SL cases and also E_a, but follow a similar trend. Similar to SL case, E_f decrease with increasing x, and they are smaller than those of pristine arsenene phases, indicating a less stable structure of ML-M_xAs with increasing cation content. Also the ordered pattern constrain brought a lower C in ML-M_xAs when compared to SL configurations. Similar crystalline to amorphous phase transition was obtained with AIMD calculations. The maximum of V_M was calculated as 0.92, 0.65, and 0.98 V for Li, Na, and K, respectively, reaching C=358 mAhg^{-1} and these are comparable with the experimental data. Trends were similar with the SL cases and ML-M_xAs phases are suitable for low charging voltage applications.

In Chapter 5, Ga and N atom adsorptions were studied for hexagonal GaN

monolayer to investigate dumbbell formation. After checking all possible adsorption sites, the most favorable was T_N for both adatoms. For Ga, T_{Ga} or T_N were energetically very similar, while for N adatoms T_N was more favorable site by 1 eV. Thus Ga-Ga and N-N geometries are considered. When single, free N adatom is approached to GaN monolayer, a dumbbell geometry (N-N DB) forms spontaneously, but in a concerted movement of two N atoms (adatom (D_1) and beneath (D_2)) and three underlying Ga atoms ($Ga_{1,2,3}$). Significant electronic charge was received by N atoms yielded three strong N-Ga bonds with a length of 2.05 Å. N atoms have stronger bonds with a bond length of 1.63 Å, and 3 + 1 coordination, while Ga atoms have four-fold coordination. DB formation process, its structure and charge transfer were very similar to the previous DB studies for germanene (Ge-Ge DB), but the bond strength was different such that dumbbell atoms ($D_{1,2}$) have stronger bonds with each other than with the nearest-neighbour sites of the lattice. Distinct dumbbell coverages of FDP (Full Dumbbell Phase), HDP (Hexagonal Dumbbell Phase), TDP (Trigonal Dumbbell Phase) and some bigger unit cells (2x2, 3x3 and 4x4) were formed. Similar coordination numbers can be obtained for low coverages, whereas five- and six-fold coordination can be observed in HDP and FDP phases. The decreasing E_b values as DBs are introduced into the monolayer indicated repulsive interaction among DBs. Cohesive energy showed a similar trend, implying that DB can be regarded as an unfavorable formation over GaN monolayer. This trend can be explained chemically by the concept of maximum coordination number. It is three for both Ga and N atoms, so they form maximum three bonds with other atoms in their compounds. In pristine GaN monolayer, each constituting Ga or N atom has three neighbours which is same as their atomic maximum coordination number. With dumbbell formationed, Ga or N atom starts having 4, 5 or 6 bonds depending on the degree of DB coverage. This concept can further explain the unfavorable energetics for Ga-Ga and N-N DB formations. A more symmetrical DB placement helps TDP phase to have larger E_c values than HDP phase. The reaction path for DB formation is analyzed by NEB calculation. The resulting small energy barrier (80 meV) for Ga to form a Ga-Ga DB indicates the possibility of DB geometry on GaN monolayer. Phonon and MD calculations indicated structural instability for FDP, HDP and TDP phases including Ga-Ga DBs. Opposite to

these, low DB coverage phases (2×2, 3×3 and 4×4) have stable structures. The structural integrity of N-N DB is studied only for 3x3 unit cell by phonon calculations, which indicated a stable structure. DB formation in general leads to spin-polarized impurity states. These are principally contributed by p-orbitals of the atoms in impurity zone (IZ) region, defined by five DB atoms. ($D_{1,2}$ $N_{1,2,3}$ for Ga-Ga DB) D_1 and D_2 atoms have sp^3-like hybridization. For Ga-Ga DB, Ga dopant involves in bonding with its three valence electrons and the system shows a semiconductor character having four localized and spin-polarized bands contributed by IZ states. Here IZ states are mainly contributed by Ga s and N p orbitals. For N-N DBs, five valence electrons of N dopant involve in bonding and the system shows metalic character. Here IZ states are mainly contributed by p orbitals. For interionic charge-transfer analysis, the effective charges calculated by Bader method indicated similar charge transfers, where each DB atoms (Ga) gives 0.69 electrons, Ga/N lattice atom donates/receives 1.37/1.37 electrons. In summary, pristine GaN monolayer having 2.15 eV band gaps becomes a metal upon N-N DB formation, while it preserves its semiconductor character but has a varying band gaps for different phases upon Ga-Ga DB formation.

Bibliography

[1] M. C. Payne, M. P. Teter, D. C. Allan, T. Arias, and a. J. Joannopoulos, "Iterative minimization techniques for ab initio total-energy calculations: molecular dynamics and conjugate gradients," *Reviews of modern physics*, vol. 64, no. 4, p. 1045, 1992.

[2] B. Delley and E. Steigmeier, "Quantum confinement in si nanocrystals," *Physical Review B*, vol. 47, no. 3, p. 1397, 1993.

[3] W. L. Wilson, P. Szajowski, and L. Brus, "Quantum confinement in size-selected, surface-oxidized silicon nanocrystals," *Science*, vol. 262, no. 5137, pp. 1242–1244, 1993.

[4] T. Takagahara and K. Takeda, "Theory of the quantum confinement effect on excitons in quantum dots of indirect-gap materials," *Physical Review B*, vol. 46, no. 23, p. 15578, 1992.

[5] K. S. Novoselov, A. K. Geim, S. V. Morozov, D. Jiang, Y. Zhang, S. V. Dubonos, I. V. Grigorieva, and A. A. Firsov, "Electric field effect in atomically thin carbon films," *science*, vol. 306, no. 5696, pp. 666–669, 2004.

[6] C. Bulutay, "Interband, intraband, and excited-state direct photon absorption of silicon and germanium nanocrystals embedded in a wide band-gap lattice," *Physical Review B*, vol. 76, no. 20, p. 205321, 2007.

[7] H. Şahin, S. Cahangirov, M. Topsakal, E. Bekaroglu, E. Akturk, R. T. Senger, and S. Ciraci, "Monolayer honeycomb structures of group-iv elements and iii-v binary compounds: First-principles calculations," *Physical Review B*, vol. 80, no. 15, p. 155453, 2009.

[8] C. Sevik, A. Kinaci, J. B. Haskins, and T. Çağın, "Characterization of thermal transport in low-dimensional boron nitride nanostructures," *Physical Review B*, vol. 84, no. 8, p. 085409, 2011.

[9] A. Onen, D. Kecik, E. Durgun, and S. Ciraci, "Gan: From three-to two-dimensional single-layer crystal and its multilayer van der waals solids," *Physical Review B*, vol. 93, no. 8, p. 085431, 2016.

[10] M. Kanli, A. Onen, A. Mogulkoc, and E. Durgun, "Characterization of two-dimensional ga1- xalxn ordered alloys with varying chemical composition," *Computational Materials Science*, vol. 167, pp. 13–18, 2019.

[11] L. Rapoport, Y. Bilik, Y. Feldman, M. Homyonfer, S. Cohen, and R. Tenne, "Hollow nanoparticles of ws 2 as potential solid-state lubricants," *Nature*, vol. 387, no. 6635, pp. 791–793, 1997.

[12] C. Lee, Q. Li, W. Kalb, X.-Z. Liu, H. Berger, R. W. Carpick, and J. Hone, "Frictional characteristics of atomically thin sheets," *science*, vol. 328, no. 5974, pp. 76–80, 2010.

[13] S. Cahangirov, C. Ataca, M. Topsakal, H. Sahin, and S. Ciraci, "Frictional figures of merit for single layered nanostructures," *Physical review letters*, vol. 108, no. 12, p. 126103, 2012.

[14] M. Y. Arsentev, A. Petrov, A. Missyul, and M. Hammouri, "Exfoliation, point defects and hydrogen storage properties of monolayer tis 3: an ab initio study," *RSC advances*, vol. 8, no. 46, pp. 26169–26179, 2018.

[15] F. Ersan, H. Ozaydin, G. Gökoğlu, and E. Aktürk, "Theoretical investigation of lithium adsorption, diffusion and coverage on mx2 (m= mo, w; x= o, s, se, te) monolayers," *Applied Surface Science*, vol. 425, pp. 301–306, 2017.

[16] L. Li, W. Wang, P. Gong, X. Zhu, B. Deng, X. Shi, G. Gao, H. Li, and T. Zhai, "2d gep: An unexploited low-symmetry semiconductor with strong in-plane anisotropy," *Advanced materials*, vol. 30, no. 14, p. 1706771, 2018.

[17] E. M. D. Siriwardane, I. Demiroglu, C. Sevik, F. M. Peeters, and D. Cakir, "Assessment of sulfur-functionalized mxenes for li-ion battery applications," *The Journal of Physical Chemistry C*, 2020.

[18] C. R. Eddy Jr, N. Nepal, J. K. Hite, and M. A. Mastro, "Perspectives on future directions in iii-n semiconductor research," *Journal of Vacuum Science & Technology A: Vacuum, Surfaces, and Films*, vol. 31, no. 5, p. 058501, 2013.

[19] J. Wu, W. Walukiewicz, K. Yu, W. Shan, J. Ager Iii, E. Haller, H. Lu, W. J. Schaff, W. Metzger, and S. Kurtz, "Superior radiation resistance of in 1- x ga x n alloys: Full-solar-spectrum photovoltaic material system," *Journal of Applied Physics*, vol. 94, no. 10, pp. 6477–6482, 2003.

[20] J. J. Williams, H. McFavilen, A. M. Fischer, D. Ding, S. R. Young, E. Vadiee, F. A. Ponce, C. Arena, C. B. Honsberg, and S. M. Goodnick, "Development of a high-band gap high temperature iii-nitride solar cell for integration with concentrated solar power technology," in *2016 IEEE 43rd Photovoltaic Specialists Conference (PVSC)*, pp. 0193–0195, IEEE, 2016.

[21] Y. Dong, B. Tian, T. J. Kempa, and C. M. Lieber, "Coaxial group iii-nitride nanowire photovoltaics," *Nano letters*, vol. 9, no. 5, pp. 2183–2187, 2009.

[22] M. A. Khan, M. Shatalov, H. Maruska, H. Wang, and E. Kuokstis, "Iii–nitride uv devices," *Japanese journal of applied physics*, vol. 44, no. 10R, p. 7191, 2005.

[23] H. Amano, Y. Baines, E. Beam, M. Borga, T. Bouchet, P. R. Chalker, M. Charles, K. J. Chen, N. Chowdhury, R. Chu, *et al.*, "The 2018 gan power electronics roadmap," *Journal of Physics D: Applied Physics*, vol. 51, no. 16, p. 163001, 2018.

[24] D. M. Kinzer and R. Beach, "Integrated iii-nitride power devices," June 23 2009. US Patent 7,550,781.

[25] H. Morkoç, *Handbook of nitride semiconductors and devices, Materials Properties, Physics and Growth*, vol. 1. John Wiley & Sons, 2009.

[26] J. Schalwig, G. Müller, O. Ambacher, and M. Stutzmann, "Group-iii-nitride based gas sensing devices," *physica status solidi (a)*, vol. 185, no. 1, pp. 39–45, 2001.

[27] C. Förster, V. Cimalla, V. Lebedev, J. Pezoldt, K. Brueckner, R. Stephan, M. Hein, E. Aperathitis, and O. Ambacher, "Group iii-nitride and sic based micro-and nanoelectromechanical resonators for sensor applications," *physica status solidi (a)*, vol. 203, no. 7, pp. 1829–1833, 2006.

[28] M. Stutzmann, G. Steinhoff, M. Eickhoff, O. Ambacher, C. Nebel, J. Schalwig, R. Neuberger, and G. Müller, "Gan-based heterostructures for sensor applications," *Diamond and related materials*, vol. 11, no. 3-6, pp. 886–891, 2002.

[29] S. Nakamura, "Nobel lecture: Background story of the invention of efficient blue ingan light emitting diodes," *Reviews of Modern Physics*, vol. 87, no. 4, p. 1139, 2015.

[30] P. Waltereit, O. Brandt, A. Trampert, H. Grahn, J. Menniger, M. Ramsteiner, M. Reiche, and K. Ploog, "Nitride semiconductors free of electrostatic fields for efficient white light-emitting diodes," *Nature*, vol. 406, no. 6798, pp. 865–868, 2000.

[31] J. J. Wierer Jr and N. Tansu, "Iii-nitride micro-leds for efficient emissive displays," *Laser & Photonics Reviews*, vol. 13, no. 9, p. 1900141, 2019.

[32] M. S. Wong, D. Hwang, A. I. Alhassan, C. Lee, R. Ley, S. Nakamura, and S. P. DenBaars, "High efficiency of iii-nitride micro-light-emitting diodes by sidewall passivation using atomic layer deposition," *Optics express*, vol. 26, no. 16, pp. 21324–21331, 2018.

[33] Z. Ren, H. Yu, Z. Liu, D. Wang, C. Xing, H. Zhang, C. Huang, S. Long, and H. Sun, "Band engineering of iii-nitride-based deep-ultraviolet light-emitting diodes: a review," *Journal of Physics D: Applied Physics*, vol. 53, no. 7, p. 073002, 2019.

[34] S. Mokkapati and C. Jagadish, "Iii-v compound sc for optoelectronic devices," *Materials Today*, vol. 12, no. 4, pp. 22–32, 2009.

[35] J. Sellés, V. Crepel, I. Roland, M. El Kurdi, X. Checoury, P. Boucaud, M. Mexis, M. Leroux, B. Damilano, S. Rennesson, *et al.*, "Iii-nitride-on-silicon microdisk lasers from the blue to the deep ultra-violet," *Applied Physics Letters*, vol. 109, no. 23, p. 231101, 2016.

[36] C. Zhao, N. Alfaraj, R. C. Subedi, J. W. Liang, A. A. Alatawi, A. A. Alhamoud, M. Ebaid, M. S. Alias, T. K. Ng, and B. S. Ooi, "Iii-nitride nanowires on unconventional substrates: From materials to optoelectronic device applications," *Progress in Quantum Electronics*, vol. 61, pp. 1–31, 2018.

[37] B. P. Yonkee, E. C. Young, C. Lee, J. T. Leonard, S. P. DenBaars, J. S. Speck, and S. Nakamura, "Demonstration of a iii-nitride edge-emitting laser diode utilizing a gan tunnel junction contact," *Optics express*, vol. 24, no. 7, pp. 7816–7822, 2016.

[38] E. Durgun, S. Tongay, and S. Ciraci, "Silicon and iii-v compound nanotubes: structural and electronic properties," *Physical Review B*, vol. 72, no. 7, p. 075420, 2005.

[39] C. Bacaksiz, H. Sahin, H. Ozaydin, S. Horzum, R. T. Senger, and F. M. Peeters, "Hexagonal aln: Dimensional-crossover-driven band-gap transition," *Physical Review B*, vol. 91, no. 8, p. 085430, 2015.

[40] H. L. Zhuang, A. K. Singh, and R. G. Hennig, "Computational discovery of single-layer iii-v materials," *Physical Review B*, vol. 87, no. 16, p. 165415, 2013.

[41] Z. Huang, T.-Y. Lü, H.-Q. Wang, S.-W. Yang, and J.-C. Zheng, "Electronic and thermoelectric properties of the group-iii nitrides (bn, aln and gan) atomic sheets under biaxial strains," *Computational Materials Science*, vol. 130, pp. 232–241, 2017.

[42] W. Auwärter, H. U. Suter, H. Sachdev, and T. Greber, "Synthesis of one monolayer of hexagonal boron nitride on ni (111) from b-trichloroborazine (clbnh) 3," *Chemistry of materials*, vol. 16, no. 2, pp. 343–345, 2004.

[43] V. Mansurov, T. Malin, Y. Galitsyn, and K. Zhuravlev, "Graphene-like aln layer formation on (111) si surface by ammonia molecular beam epitaxy," *Journal of Crystal Growth*, vol. 428, pp. 93–97, 2015.

[44] P. Tsipas, S. Kassavetis, D. Tsoutsou, E. Xenogiannopoulou, E. Golias, S. Giamini, C. Grazianetti, D. Chiappe, A. Molle, M. Fanciulli, *et al.*, "Evidence for graphite-like hexagonal aln nanosheets epitaxially grown on single crystal ag (111)," *Applied Physics Letters*, vol. 103, no. 25, p. 251605, 2013.

[45] Z. Y. Al Balushi, K. Wang, R. K. Ghosh, R. A. Vilá, S. M. Eichfeld, J. D. Caldwell, X. Qin, Y.-C. Lin, P. A. DeSario, G. Stone, *et al.*, "Two-dimensional gallium nitride realized via graphene encapsulation," *Nature materials*, vol. 15, no. 11, pp. 1166–1171, 2016.

[46] L. Li, Y. Yu, G. J. Ye, Q. Ge, X. Ou, H. Wu, D. Feng, X. H. Chen, and Y. Zhang, "Black phosphorus field-effect transistors," *Nat. Nanotech.*, vol. 9, no. 5, p. 372, 2014.

[47] Z. Zhu and D. Tománek, "Semiconducting layered blue phosphorus: a computational study," *Physical review letters*, vol. 112, no. 17, p. 176802, 2014.

[48] H. Liu, A. T. Neal, Z. Zhu, Z. Luo, X. Xu, D. Tománek, and P. D. Ye, "Phosphorene: an unexplored 2d semiconductor with a high hole mobility," *ACS nano*, vol. 8, no. 4, pp. 4033–4041, 2014.

[49] F. Xia, H. Wang, and Y. Jia, "Rediscovering black phosphorus as an anisotropic layered material for optoelectronics and electronics," *Nat. Commun.*, vol. 5, no. 1, pp. 1–6, 2014.

[50] Y. Harada, M. Yamamoto, T. Baba, and T. Kita, "Epitaxial two-dimensional nitrogen atomic sheet in gaas," *Appl. Phys. Lett.*, vol. 104, no. 4, p. 041907, 2014.

[51] H.-S. Tsai, S.-W. Wang, C.-H. Hsiao, C.-W. Chen, H. Ouyang, Y.-L. Chueh, H.-C. Kuo, and J.-H. Liang, "Direct synthesis and practical bandgap estimation of multilayer arsenene nanoribbons," *Chem. Mater.*, vol. 28, no. 2, pp. 425–429, 2016.

[52] J. Ji, X. Song, J. Liu, Z. Yan, C. Huo, S. Zhang, M. Su, L. Liao, W. Wang, Z. Ni, *et al.*, "Two-dimensional antimonene single crystals grown by van der waals epitaxy," *Nat. Commun.*, vol. 7, no. 1, pp. 1–9, 2016.

[53] F. Reis, G. Li, L. Dudy, M. Bauernfeind, S. Glass, W. Hanke, R. Thomale, J. Schäfer, and R. Claessen, "Bismuthene on a sic substrate: A candidate for a high-temperature quantum spin hall material," *Science*, vol. 357, no. 6348, pp. 287–290, 2017.

[54] V. O. Özcelik, O. Ü. Aktürk, E. Durgun, and S. Ciraci, "Prediction of a two-dimensional crystalline structure of nitrogen atoms," *Physical Review B*, vol. 92, no. 12, p. 125420, 2015.

[55] Y. Zhang, J. Lee, W.-L. Wang, and D.-X. Yao, "Two-dimensional octagon-structure monolayer of nitrogen group elements and the related nano-structures," *Comput. Mater. Sci.*, vol. 110, pp. 109–114, 2015.

[56] J. Lee, W.-C. Tian, W.-L. Wang, and D.-X. Yao, "Two-dimensional pnictogen honeycomb lattice: structure, on-site spin-orbit coupling and spin polarization," *Sci. Rep.*, vol. 5, p. 11512, 2015.

[57] S. Zhang, Z. Yan, Y. Li, Z. Chen, and H. Zeng, "Atomically thin arsenene and antimonene: semimetal–semiconductor and indirect–direct band-gap transitions," *Angew. Chem. Int. Ed.*, vol. 54, no. 10, pp. 3112–3115, 2015.

[58] C. Kamal and M. Ezawa, "Arsenene: Two-dimensional buckled and puckered honeycomb arsenic systems," *Phys. Rev. B*, vol. 91, no. 8, p. 085423, 2015.

[59] E. Aktürk, O. Ü. Aktürk, and S. Ciraci, "Single and bilayer bismuthene: Stability at high temperature and mechanical and electronic properties," *Phys. Rev. B*, vol. 94, no. 1, p. 014115, 2016.

[60] F. Ersan, D. Keçik, V. Özçelik, Y. Kadioglu, O. Ü. Aktürk, E. Durgun, E. Aktürk, and S. Ciraci, "Two-dimensional pnictogens: A review of recent progresses and future research directions," *Appl. Phys. Rev.*, vol. 6, no. 2, p. 021308, 2019.

[61] J. Su, T. Duan, W. Li, B. Xiao, G. Zhou, Y. Pei, and X. Wang, "A first-principles study of 2d antimonene electrodes for li ion storage," *Appl. Surf. Sci.*, vol. 462, pp. 270–275, 2018.

[62] W. Tian, S. Zhang, C. Huo, D. Zhu, Q. Li, L. Wang, X. Ren, L. Xie, S. Guo, P. K. Chu, *et al.*, "Few-layer antimonene: anisotropic expansion and reversible crystalline-phase evolution enable large-capacity and long-life na-ion batteries," *ACS Nano*, vol. 12, no. 2, pp. 1887–1893, 2018.

[63] W. Jin, Z. Wang, and Y. Q. Fu, "Monolayer black phosphorus as potential anode materials for mg-ion batteries," *J. Mater. Sci.*, vol. 51, no. 15, pp. 7355–7360, 2016.

[64] V. V. Kulish, O. I. Malyi, C. Persson, and P. Wu, "Phosphorene as an anode material for na-ion batteries: a first-principles study," *Phys. Chem. Chem. Phys.*, vol. 17, no. 21, pp. 13921–13928, 2015.

[65] W. Li, Y. Yang, G. Zhang, and Y.-W. Zhang, "Ultrafast and directional diffusion of lithium in phosphorene for high-performance lithium-ion battery," *Nano Lett.*, vol. 15, no. 3, pp. 1691–1697, 2015.

[66] B. Peng, H. Zhang, H. Shao, K. Xu, G. Ni, J. Li, H. Zhu, and C. M. Soukoulis, "Chemical intuition for high thermoelectric performance in monolayer black phosphorus, α-arsenene and aw-antimonene," *Journal of Materials Chemistry A*, vol. 6, no. 5, 2018.

[67] K.-X. Chen, S.-S. Lyu, X.-M. Wang, Y.-X. Fu, Y. Heng, and D.-C. Mo, "Excellent thermoelectric performance predicted in two-dimensional buckled antimonene: a first-principles study," *J. Phys. Chem. C*, vol. 121, no. 24, pp. 13035–13042, 2017.

[68] J. Dai and X. C. Zeng, "Bilayer phosphorene: effect of stacking order on bandgap and its potential applications in thin-film solar cells," *J. Phys. Chem. Lett.*, vol. 5, no. 7, pp. 1289–1293, 2014.

[69] X. Niu, Y. Li, Q. Zhou, H. Shu, and J. Wang, "Arsenene-based heterostructures: highly efficient bifunctional materials for photovoltaics and photocatalytics," *ACS applied materials & interfaces*, vol. 9, no. 49, pp. 42856–42861, 2017.

[70] D. Singh, S. K. Gupta, Y. Sonvane, and I. Lukačević, "Antimonene: a monolayer material for ultraviolet optical nanodevices," *Journal of Materials Chemistry C*, vol. 4, no. 26, pp. 6386–6390, 2016.

[71] D. Kecik, V. O. Özçelik, E. Durgun, and S. Ciraci, "Structure dependent optoelectronic properties of monolayer antimonene, bismuthene and their binary compound," *Physical Chemistry Chemical Physics*, vol. 21, no. 15, pp. 7907–7917, 2019.

[72] J. B. Goodenough, "Nobel lecture," Dec. 8 2019. https://www.nobelprize.org/prizes/chemistry/2019/goodenough/lecture/.

[73] J. Sun, H.-W. Lee, M. Pasta, H. Yuan, G. Zheng, Y. Sun, Y. Li, and Y. Cui, "A phosphorene–graphene hybrid material as a high-capacity anode for sodium-ion batteries," *Nat. Nanotech.*, vol. 10, no. 11, p. 980, 2015.

[74] S. M. Beladi-Mousavi and M. Pumera, "2d-pnictogens: alloy-based anode battery materials with ultrahigh cycling stability," *Chemical Society Reviews*, vol. 47, no. 18, pp. 6964–6989, 2018.

[75] C. Xing, L. Liu, D. Fan, Z. Peng, and H. Zhang, "Two-dimensional pnictogens, their chemistry and applications," *FlatChem*, vol. 13, pp. 8–24, 2019.

[76] C. Jellett, J. Plutnar, and M. Pumera, "Prospects for functionalizing elemental 2d pnictogens: A study of molecular models," *ACS nano*, vol. 14, no. 7, pp. 7722–7733, 2020.

[77] A. E. Del Rio Castillo, V. Pellegrini, H. Sun, J. Buha, D. A. Dinh, E. Lago, A. Ansaldo, A. Capasso, L. Manna, and F. Bonaccorso, "Exfoliation of few-layer black phosphorus in low-boiling-point solvents and its application in li-ion batteries," *Chemistry of Materials*, vol. 30, no. 2, pp. 506–516, 2018.

[78] G.-C. Guo, X.-L. Wei, D. Wang, Y. Luo, and L.-M. Liu, "Pristine and defect-containing phosphorene as promising anode materials for rechargeable li batteries," *Journal of Materials Chemistry A*, vol. 3, no. 21, pp. 11246–11252, 2015.

[79] K. Hembram, H. Jung, B. C. Yeo, S. J. Pai, S. Kim, K.-R. Lee, and S. S. Han, "Unraveling the atomistic sodiation mechanism of black phosphorus for sodium ion batteries by first-principles calculations," *The Journal of Physical Chemistry C*, vol. 119, no. 27, pp. 15041–15046, 2015.

[80] K. P. Hembram, H. Jung, B. C. Yeo, S. J. Pai, H. J. Lee, K.-R. Lee, and S. S. Han, "A comparative first-principles study of the lithiation, sodiation, and magnesiation of black phosphorus for li-, na-, and mg-ion batteries," *Physical Chemistry Chemical Physics*, vol. 18, no. 31, pp. 21391–21397, 2016.

[81] Y. Kadioglu, F. Ersan, D. Kecik, O. Ü. Aktürk, E. Aktürk, and S. Ciraci, "Chemical and substitutional doping, and anti-site and vacancy formation in monolayer aln and gan," *Physical Chemistry Chemical Physics*, vol. 20, no. 23, pp. 16077–16091, 2018.

[82] Q. Zhao, Z. Xiong, Z. Qin, L. Chen, N. Wu, and X. Li, "Tuning magnetism of monolayer gan by vacancy and nonmagnetic chemical doping," *Journal of Physics and Chemistry of Solids*, vol. 91, pp. 1–6, 2016.

[83] H. Gao, Y. Zhang, H. Ye, Z. Yu, Y. Liu, and Y. Li, "Structural and electronic properties of point defects in haeckelite gan monolayer," *Physica E: Low-dimensional Systems and Nanostructures*, vol. 103, pp. 289–293, 2018.

[84] K. H. Yeoh, K.-H. Chew, T. L. Yoon, Rusi, and D. Ong, "Strain-tunable electronic and magnetic properties of two-dimensional gallium nitride with vacancy defects," *Journal of Applied Physics*, vol. 127, no. 1, p. 015305, 2020.

[85] R. González, W. López-Pérez, Á. González-García, M. G. Moreno-Armenta, and R. González-Hernández, "Vacancy charged defects in two-dimensional gan," *Applied Surface Science*, vol. 433, pp. 1049–1055, 2018.

[86] H. Gao, H. Ye, Z. Yu, Y. Zhang, Y. Liu, and Y. Li, "Point defects and composition in hexagonal group-iii nitride monolayers: A first-principles calculation," *Superlattices and Microstructures*, vol. 112, pp. 136–142, 2017.

[87] H. Shu, X. Niu, X. Ding, and Y. Wang, "Effects of strain and surface modification on stability, electronic and optical properties of gan monolayer," *Applied Surface Science*, vol. 479, pp. 475–481, 2019.

[88] Q. Fang, Y. Huang, Y. Miao, K. Xu, Y. Li, and F. Ma, "Interfacial defect engineering on electronic states of two-dimensional aln/mos2 heterostructure," *The Journal of Physical Chemistry C*, vol. 121, no. 12, pp. 6605–6613, 2017.

[89] A. Kolobov, P. Fons, Y. Saito, J. Tominaga, B. Hyot, and B. André, "Strain engineering of atomic and electronic structures of few-monolayer-thick gan," *Physical Review Materials*, vol. 1, no. 2, p. 024003, 2017.

[90] Y. Mu, "Chemical functionalization of gan monolayer by adatom adsorption," *The Journal of Physical Chemistry C*, vol. 119, no. 36, pp. 20911–20916, 2015.

[91] W. Tang, M. Sun, J. Yu, and J.-P. Chou, "Magnetism in non-metal atoms adsorbed graphene-like gallium nitride monolayers," *Applied Surface Science*, vol. 427, pp. 609–612, 2018.

[92] Z. Cui, K. Bai, X. Wang, E. Li, and J. Zheng, "Electronic, magnetism, and optical properties of transition metals adsorbed g-gan," *Physica E: Low-dimensional Systems and Nanostructures*, vol. 118, p. 113871, 2020.

[93] V. O. Ozcelik, E. Durgun, and S. Ciraci, "New phases of germanene," *The journal of physical chemistry letters*, vol. 5, no. 15, pp. 2694–2699, 2014.

[94] S. Cahangirov, V. O. Özçelik, L. Xian, J. Avila, S. Cho, M. C. Asensio, S. Ciraci, and A. Rubio, "Atomic structure of the 3× 3 phase of silicene on ag (111)," *Physical Review B*, vol. 90, no. 3, p. 035448, 2014.

[95] V. O. Ozcelik, D. Kecik, E. Durgun, and S. Ciraci, "Adsorption of group iv elements on graphene, silicene, germanene, and stanene: dumbbell formation," *The Journal of Physical Chemistry C*, vol. 119, no. 1, pp. 845–853, 2015.

[96] E. Schrödinger, "An undulatory theory of the mechanics of atoms and molecules," *Physical review*, vol. 28, no. 6, p. 1049, 1926.

[97] L. H. Thomas, "The calculation of atomic fields," in *Mathematical Proceedings of the Cambridge Philosophical Society*, vol. 23, pp. 542–548, Cambridge University Press, 1927.

[98] E. Fermi, "Eine statistische methode zur bestimmung einiger eigenschaften des atoms und ihre anwendung auf die theorie des periodischen systems der elemente," *Zeitschrift für Physik*, vol. 48, no. 1-2, pp. 73–79, 1928.

[99] M. Born and R. Oppenheimer, "Zur quantentheorie der molekeln," *Annalen der physik*, vol. 389, no. 20, pp. 457–484, 1927.

[100] D. R. Hartree, "The wave mechanics of an atom with a non-coulomb central field. part i. theory and methods," in *Mathematical Proceedings of the Cambridge Philosophical Society*, vol. 24, pp. 89–110, 1928.

[101] V. Fock, "Näherungsmethode zur lösung des quantenmechanischen mehrkörperproblems," *Zeitschrift für Physik*, vol. 61, no. 1-2, pp. 126–148, 1930.

[102] J. C. Slater, "Note on hartree's method," *Physical Review*, vol. 35, no. 2, p. 210, 1930.

[103] P. Hohenberg and W. Kohn, "Inhomogeneous electron gas," *Physical review*, vol. 136, no. 3B, p. B864, 1964.

[104] W. Kohn and L. J. Sham, "Self-consistent equations including exchange and correlation effects," *Physical review*, vol. 140, no. 4A, p. A1133, 1965.

[105] F. Bloch, "Über die quantenmechanik der elektronen in kristallgittern," *Zeitschrift für physik*, vol. 52, no. 7-8, pp. 555–600, 1929.

[106] D. M. Ceperley and B. J. Alder, "Ground state of the electron gas by a stochastic method," *Physical Review Letters*, vol. 45, no. 7, p. 566, 1980.

[107] R. O. Jones and O. Gunnarsson, "The density functional formalism, its applications and prospects," *Reviews of Modern Physics*, vol. 61, no. 3, p. 689, 1989.

[108] J. P. Perdew and Y. Wang, "Accurate and simple analytic representation of the electron-gas correlation energy," *Physical review B*, vol. 45, no. 23, p. 13244, 1992.

[109] A. D. Becke, "A new mixing of hartree–fock and local density-functional theories," *The Journal of chemical physics*, vol. 98, no. 2, pp. 1372–1377, 1993.

[110] D. Hamann, M. Schlüter, and C. Chiang, "Norm-conserving pseudopotentials," *Physical Review Letters*, vol. 43, no. 20, p. 1494, 1979.

[111] D. Vanderbilt, "Soft self-consistent pseudopotentials in a generalized eigenvalue formalism," *Physical review B*, vol. 41, no. 11, p. 7892, 1990.

[112] R. P. Feynman, "Forces in molecules," *Physical review*, vol. 56, no. 4, p. 340, 1939.

[113] D. Kecik, A. Onen, M. Konuk, E. Gürbüz, F. Ersan, S. Cahangirov, E. Aktürk, E. Durgun, and S. Ciraci, "Fundamentals, progress, and future directions of nitride-based semiconductors and their composites in two-dimensional limit: A first-principles perspective to recent synthesis," *Applied Physics Reviews*, vol. 5, no. 1, p. 011105, 2018.

[114] Y. Ma, Y. Dai, M. Guo, C. Niu, L. Yu, and B. Huang, "Magnetic properties of the semifluorinated and semihydrogenated 2d sheets of group-iv and iii-v binary compounds," *Applied surface science*, vol. 257, no. 17, pp. 7845–7850, 2011.

[115] M. S. Prete, A. Mosca Conte, P. Gori, F. Bechstedt, and O. Pulci, "Tunable electronic properties of two-dimensional nitrides for light harvesting heterostructures," *Applied Physics Letters*, vol. 110, no. 1, p. 012103, 2017.

[116] Y. Chen, J. Xi, D. O. Dumcenco, Z. Liu, K. Suenaga, D. Wang, Z. Shuai, Y.-S. Huang, and L. Xie, "Tunable band gap photoluminescence from atomically thin transition-metal dichalcogenide alloys," *Acs Nano*, vol. 7, no. 5, pp. 4610–4616, 2013.

[117] A. Onen, D. Kecik, E. Durgun, and S. Ciraci, "In-plane commensurate gan/aln junctions: Single-layer composite structures, single and multiple quantum wells and quantum dots," *Physical Review B*, vol. 95, no. 15, p. 155435, 2017.

[118] A. Onen, D. Kecik, E. Durgun, and S. Ciraci, "Lateral and vertical heterostructures of h-gan/h-aln: electron confinement, band lineup, and quantum structures," *The Journal of Physical Chemistry C*, vol. 121, no. 48, pp. 27098–27110, 2017.

[119] F. Ersan, A. Akcay, G. Gökoğlu, and E. Aktürk, "Interactions of h-aln monolayer with platinum, oxygen, and their clusters," *Chemical Physics*, vol. 455, pp. 73–80, 2015.

[120] C. Schnohr, "Compound semiconductor alloys: From atomic-scale structure to bandgap bowing," *Applied physics reviews*, vol. 2, no. 3, p. 031304, 2015.

[121] W. Pfeiler, *Alloy physics: a comprehensive reference*. John Wiley & Sons, 2007.

[122] S. Jain, M. Willander, J. Narayan, and R. V. Overstraeten, "Iii–nitrides: Growth, characterization, and properties," *Journal of Applied Physics*, vol. 87, no. 3, pp. 965–1006, 2000.

[123] V. Wang, Z. Wu, Y. Kawazoe, and W. Geng, "Tunable band gaps of in x ga1–x n alloys: From bulk to two-dimensional limit," *The Journal of Physical Chemistry C*, vol. 122, no. 12, pp. 6930–6942, 2018.

[124] J. Kang, S. Tongay, J. Li, and J. Wu, "Monolayer semiconducting transition metal dichalcogenide alloys: Stability and band bowing," *Journal of Applied Physics*, vol. 113, no. 14, p. 143703, 2013.

[125] S. Tongay, D. S. Narang, J. Kang, W. Fan, C. Ko, A. V. Luce, K. X. Wang, J. Suh, K. Patel, V. Pathak, *et al.*, "Two-dimensional semiconductor alloys: Monolayer mo1- xwxse2," *Applied Physics Letters*, vol. 104, no. 1, p. 012101, 2014.

[126] M. Zhang, J. Wu, Y. Zhu, D. O. Dumcenco, J. Hong, N. Mao, S. Deng, Y. Chen, Y. Yang, C. Jin, *et al.*, "Two-dimensional molybdenum tungsten diselenide alloys: photoluminescence, raman scattering, and electrical transport," *ACS nano*, vol. 8, no. 7, pp. 7130–7137, 2014.

[127] H. Li, X. Duan, X. Wu, X. Zhuang, H. Zhou, Q. Zhang, X. Zhu, W. Hu, P. Ren, P. Guo, *et al.*, "Growth of alloy mos2 x se2 (1–x) nanosheets with fully tunable chemical compositions and optical properties," *Journal of the American Chemical Society*, vol. 136, no. 10, pp. 3756–3759, 2014.

[128] H.-P. Komsa and A. V. Krasheninnikov, "Two-dimensional transition metal dichalcogenide alloys: stability and electronic properties," *The journal of physical chemistry letters*, vol. 3, no. 23, pp. 3652–3656, 2012.

[129] J. Lu, K. Zhang, X. F. Liu, H. Zhang, T. C. Sum, A. H. C. Neto, and K. P. Loh, "Order–disorder transition in a two-dimensional boron–carbon–nitride alloy," *Nature communications*, vol. 4, no. 1, pp. 1–7, 2013.

[130] I. Guilhon, L. Teles, M. Marques, R. R. Pela, and F. Bechstedt, "Influence of structure and thermodynamic stability on electronic properties of two-dimensional sic, sige, and gec alloys," *Physical Review B*, vol. 92, no. 7, p. 075435, 2015.

[131] W.-x. Ji, C.-w. Zhang, M. Ding, P. Li, and P.-j. Wang, "Quantum spin hall phase transitions in two-dimensional sbbi alloy films," *Journal of Materials Chemistry C*, vol. 5, no. 10, pp. 2649–2655, 2017.

[132] J. Simon, V. Protasenko, C. Lian, H. Xing, and D. Jena, "Polarization-induced hole doping in wide–band-gap uniaxial semiconductor heterostructures," *Science*, vol. 327, no. 5961, pp. 60–64, 2010.

[133] L.-C. Duda, C. B. Stagarescu, J. Downes, K. E. Smith, D. Korakakis, T. D. Moustakas, J. Guo, and J. Nordgren, "Density of states, hybridization, and band-gap evolution in al x ga 1- x n alloys," *Physical Review B*, vol. 58, no. 4, p. 1928, 1998.

[134] L.-C. Xu, R.-Z. Wang, and H. Yan, "Order structures of al x ga1–x n alloys: First-principles predictions," *The Journal of Physical Chemistry C*, vol. 116, no. 1, pp. 1282–1285, 2012.

[135] C. Pashartis and O. Rubel, "Alloying strategy for two-dimensional gan optical emitters," *Physical Review B*, vol. 96, no. 15, p. 155209, 2017.

[136] M. Pandey, K. W. Jacobsen, and K. S. Thygesen, "Atomically thin ordered alloys of transition metal dichalcogenides: stability and band structures," *The Journal of Physical Chemistry C*, vol. 120, no. 40, pp. 23024–23029, 2016.

[137] T. L. Tan, M.-F. Ng, and G. Eda, "Stable monolayer transition metal dichalcogenide ordered alloys with tunable electronic properties," *The Journal of Physical Chemistry C*, vol. 120, no. 5, pp. 2501–2508, 2016.

[138] G. Kresse and J. Hafner, "Ab initio molecular dynamics for liquid metals," *Physical Review B*, vol. 47, no. 1, p. 558, 1993.

[139] G. Kresse and J. Hafner, "Ab initio molecular-dynamics simulation of the liquid-metal–amorphous-semiconductor transition in germanium," *Physical Review B*, vol. 49, no. 20, p. 14251, 1994.

[140] G. Kresse and J. Furthmüller, "Efficiency of ab-initio total energy calculations for metals and semiconductors using a plane-wave basis set," *Computational materials science*, vol. 6, no. 1, pp. 15–50, 1996.

[141] G. Kresse and J. Furthmüller, "Efficient iterative schemes for ab initio total-energy calculations using a plane-wave basis set," *Physical review B*, vol. 54, no. 16, p. 11169, 1996.

[142] P. E. Blöchl, "Projector augmented-wave method," *Phys. Rev. B*, vol. 50, no. 24, p. 17953, 1994.

[143] G. Kresse and D. Joubert, "From ultrasoft pseudopotentials to the projector augmented-wave method," *Physical review b*, vol. 59, no. 3, p. 1758, 1999.

[144] J. P. Perdew, K. Burke, and M. Ernzerhof, "Generalized gradient approximation made simple," *Phys. Rev. Lett.*, vol. 77, no. 18, p. 3865, 1996.

[145] H. Jónsson, G. Mills, and K. W. Jacobsen, "Nudged elastic band method for finding minimum energy paths of transitions," in *Classical and quantum dynamics in condensed phase simulations*, pp. 385–404, World Scientific, 1998.

[146] G. Henkelman, B. P. Uberuaga, and H. Jónsson, "A climbing image nudged elastic band method for finding saddle points and minimum energy paths," *J. Chem Phys.*, vol. 113, no. 22, pp. 9901–9904, 2000.

[147] G. Henkelman and H. Jónsson, "Improved tangent estimate in the nudged elastic band method for finding minimum energy paths and saddle points," *J. Chem Phys.*, vol. 113, no. 22, pp. 9978–9985, 2000.

[148] A. Togo and I. Tanaka, "First principles phonon calculations in materials science," *Scripta Mater.*, vol. 108, pp. 1–5, 2015.

[149] H. J. Monkhorst and J. D. Pack, "Special points for brillouin-zone integrations," *Phys. Rev. B*, vol. 13, no. 12, p. 5188, 1976.

[150] N. G. Limas and T. A. Manz, "Introducing ddec6 atomic population analysis: part 2. computed results for a wide range of periodic and nonperiodic materials," *RSC Adv.*, vol. 6, no. 51, pp. 45727–45747, 2016.

[151] J. Heyd, G. E. Scuseria, and M. Ernzerhof, "Hybrid functionals based on a screened coulomb potential," *J. Chem. Phys.*, vol. 118, no. 18, pp. 8207–8215, 2003.

[152] A. V. Krukau, O. A. Vydrov, A. F. Izmaylov, and G. E. Scuseria, "Influence of the exchange screening parameter on the performance of screened hybrid functionals," *J. Chem. Phys.*, vol. 125, no. 22, p. 224106, 2006.

[153] L. Vegard, "Die konstitution der mischkristalle und die raumfüllung der atome," *Z. Phys.*, vol. 5, no. 1, pp. 17–26, 1921.

[154] A. R. Denton and N. W. Ashcroft, "Vegardâ€™s law," *Phys. Rev. A*, vol. 43, no. 6, p. 3161, 1991.

[155] The calculated properties of ordered alloys are similar to the weighted averages, and obtained trends are expected to be valid for more realistic systems with random (disordered) configurations.

[156] R. Roldán, A. Castellanos-Gomez, E. Cappelluti, and F. Guinea, "Strain engineering in semiconducting two-dimensional crystals," *J. Phys.: Condens. Matter*, vol. 27, no. 31, p. 313201, 2015.

[157] D. Akinwande, C. J. Brennan, J. S. Bunch, P. Egberts, J. R. Felts, H. Gao, R. Huang, J.-S. Kim, T. Li, Y. Li, *et al.*, "A review on mechanics and mechanical properties of 2d materialsâ€"graphene and beyond," *Extreme Mech. Lett.*, vol. 13, pp. 42–77, 2017.

[158] Z. Xu, Y. Li, and Z. Liu, "First-principles calculations of structural, electronic, and thermodynamic properties of monolayer si 1- x ge x c sheet," *RSC Advances*, vol. 6, no. 115, pp. 113903–113910, 2016.

[159] A. Falin, Q. Cai, E. J. Santos, D. Scullion, D. Qian, R. Zhang, Z. Yang, S. Huang, K. Watanabe, T. Taniguchi, *et al.*, "Mechanical properties of atomically thin boron nitride and the role of interlayer interactions," *Nat. Commun.*, vol. 8, p. 15815, 2017.

[160] Y. Mogulkoc, M. Modarresi, A. Mogulkoc, and B. Alkan, "Electronic and optical properties of boron phosphide/blue phosphorus heterostructures," *Phys. Chem. Chem. Phys.*, vol. 20, no. 17, pp. 12053–12060, 2018.

[161] G. Qin, Z. Qin, H. Wang, and M. Hu, "Anomalously temperature-dependent thermal conductivity of monolayer gan with large deviations from the traditional 1/t law," *Phys. Rev. B*, vol. 95, no. 19, p. 195416, 2017.

[162] Y. Jiang, S. Cai, Y. Tao, Z. Wei, K. Bi, and Y. Chen, "Phonon transport properties of bulk and monolayer gan from first-principles calculations," *Comput. Mater. Sci.*, vol. 138, pp. 419–425, 2017.

[163] M. Kanli, M. Kurban, B. Ozdemir, A. Onen, and E. Durgun, "Single- and multi-layer arsenene as an anode material for li, na, and k-ion battery applications," *Computational Materials Science*, vol. 186, p. 110000, 2021.

[164] O. U. Akturk, E. Akturk, and S. Ciraci, "Effects of adatoms and physisorbed molecules on the physical properties of antimonene," *Phys. Rev. B*, vol. 93, no. 3, p. 035450, 2016.

[165] F. Ersan, E. Akturk, and S. Ciraci, "Interaction of adatoms and molecules with single-layer arsenene phases," *J. Phys. Chem. C*, vol. 120, no. 26, pp. 14345–14355, 2016.

[166] G. Li, Y. Zhao, S. Zeng, and J. Ni, "The realization of half-metal and spin-semiconductor for metal adatoms on arsenene," *Appl. Surf. Sci.*, vol. 390, pp. 60–67, 2016.

[167] K. Persson, V. A. Sethuraman, L. J. Hardwick, Y. Hinuma, Y. S. Meng, A. Van Der Ven, V. Srinivasan, R. Kostecki, and G. Ceder, "Lithium diffusion in graphitic carbon," *J. Phys. Chem. Lett.*, vol. 1, no. 8, pp. 1176–1180, 2010.

[168] F. Valencia, A. H. Romero, F. Ancilotto, and P. L. Silvestrelli, "Lithium adsorption on graphite from density functional theory calculations," *J. Phys. Chem. B*, vol. 110, no. 30, pp. 14832–14841, 2006.

[169] F. Ersan, G. Gokoglu, and E. Akturk, "Adsorption and diffusion of lithium on monolayer transition metal dichalcogenides (mos2 (1–x) se2 x) alloys," *J. Phys. Chem. C*, vol. 119, no. 51, pp. 28648–28653, 2015.

[170] X. Zhang, S. Li, J. Li, M. Ye, Z. Song, S. Jin, B. Shi, Y. Pan, J. Yan, Y. Wang, *et al.*, "Absorption and diffusion of lithium on layered inse," *Comput. Condens. Matter*, vol. 21, p. e00404, 2019.

[171] K. T. Chan, J. Neaton, and M. L. Cohen, "First-principles study of metal adatom adsorption on graphene," *Phys. Rev. B*, vol. 77, no. 23, p. 235430, 2008.

[172] Y. Liu, B. V. Merinov, and W. A. Goddard, "Origin of low sodium capacity in graphite and generally weak substrate binding of na and mg among alkali and alkaline earth metals," *Proc. Natl. Acad. Sci. U. S. A.*, vol. 113, no. 14, pp. 3735–3739, 2016.

[173] K. Persson, Y. Hinuma, Y. S. Meng, A. Van der Ven, and G. Ceder, "Thermodynamic and kinetic properties of the li-graphite system from first-principles calculations," *Phys. Rev. B*, vol. 82, no. 12, p. 125416, 2010.

[174] A. Sengupta and T. Frauenheim, "Lithium and sodium adsorption properties of monolayer antimonene," *Mater. Today Energy*, vol. 5, pp. 347–354, 2017.

[175] J. Wan, Y. Xu, B. Ozdemir, L. Xu, A. B. Sushkov, Z. Yang, B. Yang, D. Drew, V. Barone, and L. Hu, "Tunable broadband nanocarbon transparent conductor by electrochemical intercalation," *ACS Nano*, vol. 11, no. 1, pp. 788–796, 2017.

[176] J. Zhao, Z.-H. Qi, Y. Xu, J. Dai, X. C. Zeng, W. Guo, and J. Ma, "Theoretical studies on tunable electronic structures and potential applications of two-dimensional arsenene-based materials," *Wiley Interdiscip. Rev. Comput. Mol. Sci.*, vol. 9, no. 2, p. e1387, 2019.

[177] E. Yoo, J. Kim, E. Hosono, H.-s. Zhou, T. Kudo, and I. Honma, "Large reversible li storage of graphene nanosheet families for use in rechargeable lithium ion batteries," *Nano Lett.*, vol. 8, no. 8, pp. 2277–2282, 2008.

[178] X. Li and H. Zhu, "Two-dimensional mos2: Properties, preparation, and applications," *J. Materiomics*, vol. 1, no. 1, pp. 33–44, 2015.

[179] Q. Sun, Y. Dai, Y. Ma, T. Jing, W. Wei, and B. Huang, "Ab initio prediction and characterization of mo2c monolayer as anodes for lithium-ion and sodium-ion batteries," *J. Phys. Chem. Lett.*, vol. 7, no. 6, pp. 937–943, 2016.

[180] M. Akhtar, G. Anderson, R. Zhao, A. Alruqi, J. E. Mroczkowska, G. Sumanasekera, and J. B. Jasinski, "Recent advances in synthesis, properties, and applications of phosphorene," *npj 2D Mater. Appl.*, vol. 1, no. 1, p. 5, 2017.

[181] J. Zhou, Q. Sun, Q. Wang, and P. Jena, "Tailoring li adsorption on graphene," *Phys. Rev. B*, vol. 90, no. 20, p. 205427, 2014.

[182] Q. Zhou, W. Ju, Y. Yong, and X. Li, "Electronic and magnetic properties of 3d transition-metal atom adsorbed vacancy-defected arsenene: A first-principles study," *Journal of Magnetism and Magnetic Materials*, vol. 491, p. 165613, 2019.

[183] Q. Zhou, W. Ju, Y. Liu, J. Li, and Q. Zhang, "Influence of defects and dopants on the sensitivity of arsenene towards hcn," *Applied Surface Science*, vol. 506, p. 144936, 2020.

[184] Y. R. Lim, F. Shojaei, K. Park, C. S. Jung, J. Park, W. I. Cho, and H. S. Kang, "Arsenic for high-capacity lithium-and sodium-ion batteries," *Nanoscale*, vol. 10, no. 15, pp. 7047–7057, 2018.

[185] H. Benzidi, M. Lakhal, M. Garara, M. Abdellaoui, A. Benyoussef, O. Mounkachi, *et al.*, "Arsenene monolayer as an outstanding anode material for (li/na/mg)-ion batteries: density functional theory," *PCCP*, vol. 21, no. 36, pp. 19951–19962, 2019.

[186] B. Akgenc, "Two-dimensional black arsenic for li-ion battery applications: a dft study," *J. Mater. Sci.*, vol. 54, no. 13, pp. 9543–9552, 2019.

[187] S. Grimme, J. Antony, S. Ehrlich, and H. Krieg, "A consistent and accurate ab initio parametrization of density functional dispersion correction (dft-d) for the 94 elements h-pu," *J. Chem. Phys.*, vol. 132, no. 15, p. 154104, 2010.

[188] S. Grimme, S. Ehrlich, and L. Goerigk, "Effect of the damping function in dispersion corrected density functional theory," *J. Comput. Chem.y*, vol. 32, no. 7, pp. 1456–1465, 2011.

[189] M. Aydinol, A. Kohan, and G. Ceder, "Ab initio calculation of the intercalation voltage of lithium-transition-metal oxide electrodes for rechargeable batteries," *J. Power Sources*, vol. 68, no. 2, pp. 664–668, 1997.

[190] D. Kecik, E. Durgun, and S. Ciraci, "Stability of single-layer and multilayer arsenene and their mechanical and electronic properties," *Phys. Rev. B*, vol. 94, no. 20, p. 205409, 2016.

[191] Y. Liu, V. I. Artyukhov, M. Liu, A. R. Harutyunyan, and B. I. Yakobson, "Feasibility of lithium storage on graphene and its derivatives," *J. Phys. Chem. Lett.*, vol. 4, no. 10, pp. 1737–1742, 2013.

[192] L. Shi and T. Zhao, "Recent advances in inorganic 2d materials and their applications in lithium and sodium batteries," *J. Mater. Chem. A*, vol. 5, no. 8, pp. 3735–3758, 2017.

[193] G.-C. Guo, D. Wang, X.-L. Wei, Q. Zhang, H. Liu, W.-M. Lau, and L.-M. Liu, "First-principles study of phosphorene and graphene heterostructure as anode materials for rechargeable li batteries," *J. Phys. Chem. Lett.*, vol. 6, no. 24, pp. 5002–5008, 2015.

[194] S. Zhao, W. Kang, and J. Xue, "The potential application of phosphorene as an anode material in li-ion batteries," *J. Mater. Chem. A*, vol. 2, no. 44, pp. 19046–19052, 2014.

[195] A. Nie, Y. Cheng, S. Ning, T. Foroozan, P. Yasaei, W. Li, B. Song, Y. Yuan, L. Chen, A. Salehi-Khojin, F. Mashayek, and R. Shahbazian-Yassar, "Selective ionic transport pathways in phosphorene," *Nano Lett.*, vol. 16, no. 4, pp. 2240–2247, 2016.

[196] B. Mortazavi, A. Dianat, G. Cuniberti, and T. Rabczuk, "Application of silicene, germanene and stanene for na or li ion storage: A theoretical investigation," *Electrochim. Acta*, vol. 213, pp. 865–870, 2016.

[197] Y. Jing, Z. Zhou, C. R. Cabrera, and Z. Chen, "Metallic vs2 monolayer: A promising 2d anode material for lithium ion batteries," *J. Phys. Chem. C*, vol. 117, no. 48, pp. 25409–25413, 2013.

[198] C. Uthaisar and V. Barone, "Edge effects on the characteristics of li diffusion in graphene," *Nano Lett.*, vol. 10, no. 8, pp. 2838–2842, 2010.

[199] W. Zhang, Y. Liu, and Z. Guo, "Approaching high-performance potassium-ion batteries via advanced design strategies and engineering," *Sci. Adv.*, vol. 5, no. 5, p. eaav7412, 2019.

[200] S. Mukherjee, L. Kavalsky, and C. V. Singh, "Ultrahigh storage and fast diffusion of na and k in blue phosphorene anodes," *ACS Appl. Mater. Interfaces*, vol. 10, no. 10, pp. 8630–8639, 2018.

[201] W. Luo, J. Wan, B. Ozdemir, W. Bao, Y. Chen, J. Dai, H. Lin, Y. Xu, F. Gu, V. Barone, *et al.*, "Potassium ion batteries with graphitic materials," *Nano Lett.*, vol. 15, no. 11, pp. 7671–7677, 2015.

[202] R. P. Joshi, B. Ozdemir, V. Barone, and J. E. Peralta, "Hexagonal bc3: A robust electrode material for li, na, and k ion batteries," *J. Phys. Chem. Lett.*, vol. 6, no. 14, pp. 2728–2732, 2015.

[203] Z. Yang, D. Choi, S. Kerisit, K. M. Rosso, D. Wang, J. Zhang, G. Graff, and J. Liu, "Nanostructures and lithium electrochemical reactivity of lithium titanites and titanium oxides: A review," *J. Power Sources*, vol. 192, no. 2, pp. 588–598, 2009.

[204] M. Mortazavi, C. Wang, J. Deng, V. B. Shenoy, and N. V. Medhekar, "Ab initio characterization of layered mos2 as anode for sodium-ion batteries," *J. Power Sources*, vol. 268, pp. 279–286, 2014.

[205] D. Cakir, C. Sevik, O. Gulseren, and F. M. Peeters, "Mo2c as a high capacity anode material: a first-principles study," *J. Mater. Chem. A*, vol. 4, pp. 6029–6035, 2016.

[206] Z. Cui, X. Wang, E. Li, Y. Ding, C. Sun, and M. Sun, "Alkali-metal-adsorbed g-gan monolayer: ultralow work functions and optical properties," *Nanoscale research letters*, vol. 13, no. 1, pp. 1–9, 2018.

[207] E. Sanville, S. D. Kenny, R. Smith, and G. Henkelman, "Improved grid-based algorithm for bader charge allocation," *Journal of computational chemistry*, vol. 28, no. 5, pp. 899–908, 2007.